



Norwegian University of  
Science and Technology

# Fatigue Assessment of AZ31 Magnesium Alloy Weldments

Application of a Local Energy-Based Method

**Emil Scott Bale**

Master of Science in Mechanical Engineering

Submission date: June 2018

Supervisor: Filippo Berto, MTP

Co-supervisor: Seyed Mohammad Javad Razavi, MTP

Norwegian University of Science and Technology  
Department of Mechanical and Industrial Engineering



---

# Abstract

Traditional stress-based fatigue criteria are highly dependent of geometry and loading mode and are often based on idealized geometries and loading conditions. These fatigue criteria are seldom applicable in general engineering assessments of structural components.

The scope of the thesis is therefore to apply the energy-based fatigue criterion of *average local strain energy density* (ASED) to welded joints of AZ31 magnesium alloy. A fatigue criterion which is both geometry and loading mode independent. The application of ASED as a new criterion was based on experimentally gathered fatigue data for three different weld geometries, namely: fully penetrated butt welded plate; non-penetrated butt welded plate; plate with a welded transverse stiffener. These three geometries were subjected to three different loading ratios of  $R=-1$ ,  $R=0$ , and  $R=0.5$ .

Application of ASED criterion was performed with the aid of a numerical investigation using the Computer Aided Engineering (CAE) software Abaqus 6-14. Finite element models were constructed to best represent the actual occurring constraints, which were applied to the experimental specimens during testing. The models were then subjected to the stress range ( $\Delta\sigma$ ) used experimentally.

The control radius ( $R_c$ ) which defines the in-closed volume used in the fatigue evaluation, was found with the aid of a "best-fit" approach. Fatigue data from the three geometries under  $R=0$  loading were tested with incrementally changing  $R_c$ . The  $R_c$  that yielded the best regression fit was select to be the appropriate one, resulting in the selection of  $R_c = 0.15 \text{ mm}$ .

In addition to the numerical investigation, an analytical evaluation of ASED was performed to compare the results with the FEM results. Through this evaluation it was found that the discrepancy between calculating ASED from the stress intensity factor (SIF, which is found through fine mesh FEM) and the extracted ASED was at 11.8%. It is important to mention that SIF was extracted by using  $\sim 1500$  elements, and ASED with 40, which gives a ratio of 1 : 37.5.

---

---

---

# Samandrag

Tradisjonelle stressbaserte utmattingskriterium er svært avhengige av geometri og belastingsmodus, og er ofte basert på idealiserte geometriar og belastningar. Desse utmattingskriteria er sjeldan brukbare i generelle tekniske vurderingar av strukturelle komponentar.

Målet med masteroppgåva er å nytte det energibaserte utmattingskriterie: Lokal gjennomsnittleg tøyingsenergi tettheit<sup>1</sup> (ASED) på sveisesambindingar av AZ31 magnesiumlegering. Frå tidlegare har dette kriteriet vist seg å vere både geometri og belastingsretning uavhengig. Bruken av ASED som eit nytt kriterium blir i masteroppgåva basert på eksperimentelt innsamla utmattingsdata for tre forskjellige sveisegeometriar: fullt gjennombrent buttsveisa plate, ikkje-gjennombrent buttsveisa plate og plate med kilesveisa transversellavstivar. Desse tre geometriane blei utsett for tre ulike belastningsratioar nemleg,  $R = -1$ ,  $R = 0$  og  $R = 0.5$ .

Applikasjon av ASED kriteriet blei utført ved hjelp av numeriske undersøkingar gjennom CAE programvara Abaqus 6-14. Elementmetodemodellane blei konstruerte slik at dei best mogeleg kunne representere dei faktiske belastningane som prøvestykkane blei utsette for under den eksperimentelle testinga.

Kontrollradiusen ( $R_c$ ) som definerer det lukka volumet brukt i utrekninga av  $\Delta\bar{W}$ , blei funne ved hjelp av ei "best-fit" tilnærming. Utmattingsdata frå dei tre geometriane under  $R = 0$ -belastninga blei analyserte med trinnvis skiftande kontrollradius. Kontrollradiusen som ga den beste potensregresjonen, blei valt til å vere den ideelle, noko som resulterte i valet av kontrollradiusen  $R_c = 0.15\text{mm}$ .

I tillegg til dei numeriske undersøkingane blei det utført analytiske evalueringar av bruken av ASED. Desse evalueringane fann at avviket mellom utrekninga av ASED frå stressintensitetsfaktoren (SIF, som blei funne gjennom finelementanalysar) samanlikna med ekstrahert ASED var på 11,8%. Det er viktig å erkjenne at SIF blei ekstrahert ved bruka av 1500 element, medan ASED brukte 40. Noko som gir eit forhold på 1: 37.5.

---

<sup>1</sup> Average Local Strain Energy Density,  $\Delta\bar{W}$

---

---

# Preface

The presented work in this Master's thesis has been conducted at the Norwegian University of Science and Technology (NTNU) as part of the two-year Master's degree program *Mechanical Engineering* with a specialization in *Product Development and Materials Engineering*. Work presented was conducted by the author at the Department of Mechanical and Industrial Engineering as a member of the Materials Design and Compliance group. The project duration was 20 weeks in the spring semester of 2018.

The problem description was drafted in collaboration with supervisor Professor Filippo Berto and co-supervisor PhD. student Seyed Mohammad Javad Razavi. Özler Karakaş supplied the experimental data considered in this thesis.

.....  
Emil Scott Bale  
Trondheim  
June 10, 2018

---

---

# Acknowledgements

I would like to use this opportunity to thank my supervisor Professor Filippo Berto and co-supervisor Ph.D. student Seyed Mohammad Javad Razavi for developing the thesis and aiding me through this project. I would particularly like to highlight the help from Mr. Razavi, as he has been of excellent support through the project period and a highly valued interlocutor. I would also like to thank my family, for taking an interest in the work I have put down this semester, and for the support, they have given me. Lastly, I would like to give a heartfelt thanks to my girlfriend. She has given me the support I need during this project, as well as playing an essential role in aiding me in the final stages of this endeavor.

---

# Table of Contents

<b>Abstract</b>	<b>i</b>
<b>Samandrag</b>	<b>iii</b>
<b>Preface</b>	<b>v</b>
<b>Acknowledgements</b>	<b>vii</b>
<b>Table of Contents</b>	<b>x</b>
<b>List of Tables</b>	<b>xi</b>
<b>List of Figures</b>	<b>xiv</b>
<b>Abbreviations and Nomenclature</b>	<b>xv</b>
<b>1 Introduction</b>	<b>1</b>
1.1 Background and Motivation . . . . .	1
1.2 Problem Description . . . . .	2
1.3 Project Scope . . . . .	2
1.3.1 Objective . . . . .	2
1.3.2 Research Questions . . . . .	2
1.3.3 Limitations . . . . .	3
1.4 Thesis Structure . . . . .	3
<b>2 Theory</b>	<b>5</b>
2.1 Basics of Fatigue . . . . .	5
2.2 Welding and Welded Joints . . . . .	6
2.2.1 Welding Techniques . . . . .	6
2.2.2 Weld Geometries . . . . .	8
2.3 Fracture Mechanics . . . . .	9
2.3.1 Basics of Fracture Mechanic . . . . .	9
2.3.2 Cracks versus Notches . . . . .	12
2.3.3 Strain Energy Density . . . . .	14
2.4 Magnesium and AZ31 Magnesium Alloy . . . . .	17
<b>3 Literature review</b>	<b>19</b>
3.1 AZ31 Magnesium Alloy . . . . .	19
3.1.1 Fatigue of Welded Magnesium Alloy Joints . . . . .	19
3.1.2 Critical distance approach for the fatigue strength assessment of magnesium welded joints in contrast with Neuber’s effective stress method . . . . .	21
3.2 Local Strain Energy Density . . . . .	23

---

3.2.1	Fatigue strength of steel and aluminum welded joints based on generalised stress intensity factors and local strain energy values .	23
<b>4</b>	<b>Methodology</b>	<b>27</b>
4.1	Experimental Procedure . . . . .	27
4.2	Numerical Procedure . . . . .	31
4.2.1	Finite Element Method Model . . . . .	32
4.3	Analytical Evaluation . . . . .	40
4.3.1	An analytical approach to ASED . . . . .	40
4.3.2	An analytical approach to determine maximum blunt notch stress from $\bar{W}$ . . . . .	42
<b>5</b>	<b>Results</b>	<b>45</b>
5.1	Experimental Results . . . . .	45
5.2	Numerical Results . . . . .	47
5.3	Analytical Results . . . . .	51
<b>6</b>	<b>Discussion</b>	<b>53</b>
<b>7</b>	<b>Conclusion</b>	<b>59</b>
7.1	Further work . . . . .	60
	<b>Bibliography</b>	<b>61</b>
	<b>Appendix</b>	<b>65</b>
<b>A</b>	<b>Notch opening angle variables</b>	<b>67</b>
<b>B</b>	<b>AZ31 Magnesium Alloy material properties</b>	<b>69</b>
<b>C</b>	<b>Experimental and numerical results</b>	<b>71</b>
<b>D</b>	<b>Results from analytical investigation</b>	<b>79</b>

# List of Tables

2.1	Fatigue parameters . . . . .	5
2.2	Magnesium alloy designations . . . . .	17
2.3	Chemical composition of AZ31 magnesium alloy . . . . .	18
2.4	AZ31 magnesium alloy material properties . . . . .	18
3.1	Scatter values of all determined S-N curves . . . . .	22
4.1	Tested specimens . . . . .	27
4.2	Process-specific parameters and procedures of MIG “Triggered Short Arc” for the fully penetrated butt welded plates . . . . .	28
4.3	Process-specific parameters and procedures of TIG for the non-penetrated butt welded plates . . . . .	28
4.4	Process-specific parameters and procedures of MIG “Triggered Short Arc” for the plates with welded transverse stiffener . . . . .	29
4.5	Blunt notch compensation parameters . . . . .	35
4.6	Number of elements within control radius of FEM models . . . . .	40
5.1	Numerically and analytically derived weld toe max stress for the fully penetrated butt welded plate . . . . .	51
6.1	Fatigue strength at $N_f = 2 \cdot 10^6$ . . . . .	53
A.1	Notch opening angle variables . . . . .	67
B.1	Monotonic and cyclic material properties of AZ31 magnesium alloy . . . . .	69
C.1	Fully penetrated butt welded plate, R = -1 . . . . .	71
C.2	Fully penetrated butt welded plate, R = 0 . . . . .	72
C.3	Fully penetrated butt welded plate, R = 0.5 . . . . .	72
C.4	Non-penetrated butt welded plate, R = -1 . . . . .	73
C.5	Non-penetrated butt welded plate, R = 0 . . . . .	74
C.6	Non-penetrated butt welded plate, R = 0.5 . . . . .	75
C.7	Plate with welded transverse stiffener, R = -1 . . . . .	76
C.8	Plate with welded transverse stiffener, R = 0 . . . . .	77
C.9	Plate with welded transverse stiffener, R = 0.5 . . . . .	78
D.1	Analytical results for non-penetrated butt welded plate, R=-1 . . . . .	79
D.2	Analytical results for non-penetrated butt welded plate, R=0 . . . . .	80
D.3	Analytical results for non-penetrated butt welded plate, R=0.5 . . . . .	80

---

# List of Figures

2.1	Cyclic loading with constant amplitude, frequency and waveform . . . . .	5
2.2	Heat-affected zone in butt welded plate . . . . .	7
2.3	Illustration of MIG and TIG welding techniques . . . . .	8
2.4	Important weld geometry terminology . . . . .	8
2.5	Difference between LEFM and EPFM in regards to crack tip stress field .	9
2.6	Fracture modes . . . . .	10
2.7	Blunt v-notch, with common designations . . . . .	12
2.8	Plot of equation 2.10 for mode I and mode II loading, $\lambda_I$ and $\lambda_{II}$ as a function of notch opening angle $2\alpha$ . . . . .	13
2.9	Control radius on sharp V-notch and a blunt tip V-notch . . . . .	15
2.10	Plot of $\Delta\bar{W}$ vs. $N_f$ for different steel geometries. . . . .	16
3.1	Microstructures of welded joints of AZ31 . . . . .	20
3.2	Representation of the stress averaging method (a) and the critical distance method (b) . . . . .	21
3.3	Resulting S-N curves using the critical distance method for both radii considered. . . . .	22
3.4	Geometrical parameters and critical volume (area) at the weld toe and root	23
3.5	Strain energy-based scatter band summarizing fatigue strength of welded steel and aluminum joints . . . . .	24
3.6	Strain energy-based scatter bands summarizing about 650 fatigue data of welded joints made of steel and aluminum subjected to tension and bending loads. . . . .	25
4.1	Picture of welded experimental specimens. . . . .	29
4.2	Mean experimental specimen dimensions . . . . .	30
4.3	Measures weld seam hardness distribution . . . . .	31
4.4	Model simplification . . . . .	32
4.5	Boundary conditions and load application to FEM models . . . . .	33
4.6	Notch opening angle ( $2\alpha$ ) for fully penetrated butt welded plate . . . . .	35
4.7	Meshed geometries. From top: fully penetrated butt welded plate, non-penetrated butt welded plate and plate with welded traversal stiffener where the control radius, $R_c$ is highlighted . . . . .	35
4.8	Placement of control radius for fully penetrated butt welded plate . . . . .	36
4.9	Placement of control radius for non-penetrated butt welded plate . . . . .	36
4.10	Placement of control radius for plate with welded traversal stiffener . . . . .	36
4.11	Resulting data scatter with incrementally changing $R_c$ , for welded specimens under $R = 0$ loading. FP: Fully penetrated butt welded plate; NP: Non-penetrated butt welded plate; TS: Plate with welded transverse stiffener	38
4.12	Effect of the number of elements in the control radius, $R_c$ . . . . .	39
4.13	Mesh sensitivity of SIF the weld root of the non-penetrated welded plate under a unit load of 1 MPa . . . . .	41

---

4.14	Coarse to fine mesh, weld root . . . . .	42
4.15	Maximum orthogonal stress relative to centre of notch and the notch bi-sector line $\gamma$ . . . . .	43
4.16	Coarse to fine mesh, weld toe . . . . .	43
4.17	Number of elements vs. resulting orthogonal max stress . . . . .	44
5.1	Failure points of the welded experimental specimens . . . . .	45
5.2	S-N curves for welded joints of AZ31 magnesium alloy under fully reversed loading, R=-1 . . . . .	45
5.3	S-N curves for welded joints of AZ31 magnesium alloy under pulsating loading, R=0 . . . . .	46
5.4	S-N curves for welded joints of AZ31 magnesium alloy under high mean stress, R=0.5 . . . . .	46
5.5	$\Delta\bar{W}$ - N curve for welded joints of AZ31 magnesium alloy under fully reversed loading, R=-1 . . . . .	47
5.6	$\Delta\bar{W}$ - N curve for welded joints of AZ31 magnesium alloy under pulsating loading, R=0 . . . . .	48
5.7	$\Delta\bar{W}$ - N curve for welded joints of AZ31 magnesium alloy under high mean stress, R=0.5 . . . . .	48
5.8	$\Delta\bar{W}$ - N curve for fully penetrated butt welded plate regardless of mean stress . . . . .	49
5.9	$\Delta\bar{W}$ - N curve for non-penetrated butt welded plate regardless of mean stress . . . . .	49
5.10	$\Delta\bar{W}$ - N curve for plate with welded transverse stiffener regardless of mean stress . . . . .	50
5.11	$\Delta\bar{W}$ - N curve for welded joints of AZ31 magnesium alloy regardless of loading ratio . . . . .	50
5.12	Analytically derived $\Delta\bar{W}$ - N curve for non-penetrated butt welded plate . . . . .	51
6.1	Comparison of $\Delta\bar{W} - N_f$ for AZ31 magnesium alloy and regression line for welded aluminum joints . . . . .	55
6.2	Comparison of analytically derived $\Delta\bar{W} - N_f$ and numerically derived $\Delta\bar{W} - N_f$ . . . . .	57
6.3	Plot of the effect of altering the control radius on the resultant $\Delta\bar{W}$ when specimens are applied with their respective fatigue strength at $N_f = 2 \cdot 10^6$ at R=0 . . . . .	58

---

# Abbreviations and Nomenclature

## Abbreviations

AC	Alternating Current
ASED	Average Strain Energy Density
CEA	Computer Aided Engineering
DC	Direct Current
ELSE	Total elastic strain energy in an element
EPFM	Elastic-Plastic Fracture Mechanics
EVOL	Element volume
FEA	Finite Element Analysis
FEM	Finite Element Method
HAZ	Heat Effected Zone
LEFM	Linear Elastic Fracture Mechanics
MIG	Metal Inert Gas welding
NSIF	Notch Stress Intensity Factor
SED	Strain Energy Density
SIF	Stress Intensity Factor
TIG	Tungsten Inert Gas welding

---

## Nomenclature

$a$	Crack length
$\Delta\sigma$	Stress range
$E$	Modulus of elasticity/Young's modulus
$\gamma$	Notch bisector line
$K_{Ic}$	Fracture toughness
$K_I$	Stress Intensity Factor for <i>mode I</i> loading
$\Delta K_1$	SIF range for <i>mode I</i> loading
$\lambda_I$	Notch opening parameter for <i>mode I</i> loading
$\lambda_{II}$	Notch opening parameter for <i>mode II</i> loading
$G_{Ic}$	Critical energy release rate
$\sigma_{max}$	Maximum orthogonal stress relative to the notch bisector
$N_f$	Number of cycles to failure
$\rho$	Blunt notch tip radius
$\Delta\sigma_{a,nom}$	Nominal stress amplitude
$2\alpha$	Notch opening angle
$\nu$	Poisson ratio
$R$	Stress ratio
$r_0$	Blunt notch compensation factor
$R_c$	Control Radius
$R^2$	Coefficient of determination
$\overline{W}_c$	Critical SED
$\Delta\overline{W}$	Average Strain Energy Density range
$\overline{W}$	Average Strain Energy Density
$T_{\Delta\overline{W}}$	SED based scatter parameter
$t$	Specimen thickness
$T_\sigma$	Stress based scatter parameter

# Chapter 1

## Introduction

### 1.1 Background and Motivation

The United Nations have projected that the human population will grow from today's estimate of 7 billion people and reach 10.1 billion by the year 2100 [1]. As the growth of the population is gradually increasing, the demand for building new and larger structures both for housing and for infrastructures will increase alongside it. To sustain the construction of such large structures, the use of traditional building materials will not be sufficient, and a need for new materials will arise.

In later years, an interest for using low mass density and high strength materials have increased. Common for the use of such materials is that they can reduce the structure's specific weight, and at the same time maintain the strength when compared with traditional building materials, such as e.g., steel. Before implementing these new lightweight and high strength materials, it is essential to understand how they will sustain over time. One of these materials is magnesium alloys. Traditionally magnesium alloys have mainly been used in the aerospace and automobile industry, where joining methods as riveting, bolting and adhesive joining is common. The joining method of welding is also popular for magnesium alloys. Welding, although a robust and efficient joining method can cause problems such as stress concentrations, internal defects, and cracks. Especially the stress concentrations cause by the weld geometry are problematic for components designed of a long lifespan, as they are prone to fatigue.

The phenomenon of fatigue or cyclic loading is one of the most common causes for mechanical or structural components to fail. A failure caused by fatigue generally happens without any form of prior notice and is therefore often considered as one of the most critical failure modes. An example of the consequences of fatigue failure is the story of the aircraft *De Havilland DH106 Comet I*. The *Comet I* entered commercial service in 1952 and was the first commercial aircraft to be jet propelled. After just a few years in service, a number of accidents under similar circumstances occurred. Studies of the wreckage and fracture mechanical investigations of the fuselage were performed. It was concluded with that Comet I's large rectangular shaped windows had generated large stress concentrations in its corners as the pressure-cabin was pressurized during flight. Repetitively pressurization in combination with the resultant stress concentrations resulted in fatigue of the airframe, and ultimately to full failure as the fuselage ruptured in mid-flight. [2]

Traditional approaches for assessing the service life of a structure under cyclic loading depends highly on idealized geometries under particular loading conditions. This makes the traditional approaches seldom applicable in a general engineering assessment of a structural component. In later years a new fatigue criterion has been developed called *Average Local strain energy density* (ASED). The use of ASED as a fatigue criterion of welded

steel and aluminum alloys have been widely investigated in the later years. ASED is an approach that, instead of having its base in stress (as most traditional approaches), is based on the local strain energy surrounding the stress concentrations caused by for example a weld. This method makes it possible to have a fatigue criterion that is more or less geometry and load direction independent, which gives a fatigue assessment solely based on material properties. [3, 4, 5]

## 1.2 Problem Description

The main aim of this project is to assess the fatigue behaviour of welded joints made of AZ31 magnesium alloy tested under various loading conditions using an energy-based criterion namely the *Average Strain Energy Density* (ASED) criterion. Fatigue behaviour of the welded structural connections is to be studied experimentally and theoretically on the standard specimens subjected to different loading conditions. The ability of the theoretical failure criterion for predicting the fatigue life of the tested specimens will be evaluated as a final goal.

## 1.3 Project Scope

### 1.3.1 Objective

The objective of the work conducted in this thesis is to assess the applicability of ASED as a criterion for predicting the fatigue life of welded joints made of AZ31 magnesium alloy. The assessment is based on experimentally gathered fatigue data for three different joint geometries, which have been tested at three different loading ratios. In addition to the numerical investigation, an analytical evaluation is to be performed. This is to give insight into the parameters used and the applicability of formulations found in the literature.

### 1.3.2 Research Questions

The main research questions studied in this thesis are:

- How will the geometry and loading ratio affect the fatigue life of weldments made from AZ31 magnesium alloy?
- Will the fatigue criterion of *ASED* derived through numerical assessments be applicable to weldments made of AZ31 magnesium alloy?
- Are formulations for *ASED* found in the literature applicable for AZ31 magnesium alloy?

### 1.3.3 Limitations

The main limitation concerning this project is that all experimental data is supplied by an external source in open literature. The limitations is therefore that the accuracy of the application of ASED as a fatigue criterion heavily depends on the accuracy of the received experimental results.

## 1.4 Thesis Structure

The thesis is divided into six main parts, namely: Theory; Literature review; Methodology; Result; Discussion; Conclusion. In the Theory section of the thesis, the objective is to present relevant theory to the topic of the thesis, so that a reader with basic knowledge of material and mechanical engineering can perceive the main topic, Methodology, Result, and Conclusion. In the Literature Review section of the thesis, a presentation of "*state of the art*" research and publications on topics relevant to the thesis is presented. This is so that the scope, Methodology, and Results can be put into context with the existing research.

The Methodology section presents the procedures for experimental, numerical and analytical evaluation of the fatigue properties of welded AZ31 magnesium alloy and the application of ASED as a fatigue criterion. This is so that all results presented in this thesis are to be repeatable if the same conditions, methodology, and procedures are followed. Also included in this section is an evaluation of the selected parameters used in the numerical models. This evaluation is based on comparing numerical results with results found analytically through the use of equations from the literature.

In the Result and Discussion sections, there is a presentation of the results found when following the procedure presented in the Methodology section. In addition, the viability of the results and method of result acquirement will be discussed and compared to similar researches found in published literature. The thesis ends with a conclusion where the work that is done and the results are put into perspective as a conclusion drawn. In addition, a "further work" section is added, to give some general guidelines for further research on the topic.



# Chapter 2

## Theory

### 2.1 Basics of Fatigue

There are various ways of simulating fatigue behaviour in a structural component. Regardless, their main goal is generally based in estimating the number of load cycles before an event (failure or micro-cracks initiation), or determining the rate of crack propagation (the rate of change in crack length) [6]. When a material and/or a geometrie's resistance to fatigue (fatigue properties) is investigated experimentally, the terms and parameters often used are illustrated and described by figure 2.1 and table 2.1. In figure 2.1, the loading and unloading follow a sine waveform. However, there are multiple wave-forms that can be utilised such as sawtooth, square, pike, etc. Also in figure 2.1, both the  $\sigma_{max}$  and  $\sigma_{min}$  have positive values and results in an  $R > 0$ , this is called *tension-tension*.  $R$  is the loading ratio, and describes the relationship between the maximum occurring nominal stress and the minimum. Another common loading pattern is fully reversed loading, where  $\sigma_{min} = -\sigma_{max}$  and hence  $R = -1$ .

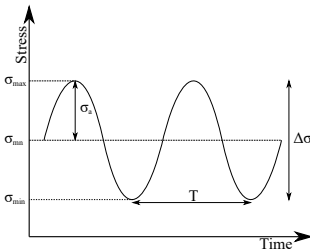


**Table 2.1:** Fatigue parameters

Maximum stress	$\sigma_{max}$ [MPa]
Minimum stress	$\sigma_{min}$ [MPa]
Stress amplitude	$\sigma_a = \frac{\sigma_{max} - \sigma_{min}}{2}$ [MPa]
Mean stress	$\sigma_{mn} = \frac{\sigma_{max} + \sigma_{min}}{2}$ [MPa]
Stress range	$\Delta S = S_{max} - S_{min}$ [MPa]
Stress ratio	$R = \frac{\sigma_{min}}{\sigma_{max}}$
Period	$T$ [sec]
Frequency	$f = \frac{1}{T}$ [Hz]

**Figure 2.1:** Cyclic loading with constant amplitude, frequency and waveform

In the life of a structural component, the loading seldom has a constant amplitude and/or pattern. It may, therefore, be difficult to estimate expected fatigue life. One method for modelling fatigue life under variable loading is by the use of *Cumulative Damage Loading*. One approach to this is through the use of Palmgren-Miner rule. It proposes that a body can tolerate a predetermined amount of damage  $D_i$  ( $i = 1, \dots, N$ ). Failure will then occur when the sum of damage ( $D$ ) is equal to that of the predetermined damage resistance (see eq. 2.1). [7]

$$\sum_{i=1}^N \frac{D_i}{D} = 1 \quad (2.1)$$

To obtain sufficient data to predict fatigue behaviour of a specific material and/or geometry under a set of predetermined conditions, multiple specimens have to be tested at various stress levels and the number of cycles at failure recorded. This data can then be plotted

to generate, for instance, a Wöler S-N curve (stress to numbers of cycles to failure curve), and then a function for fatigue life may be fitted to it. There are various approaches to determine a fatigue life function. Equation 2.2 uses the stress-life approach for fully reversed loading ( $R = -1$ )[7].

$$\sigma_a = AN_f^\alpha \quad (2.2)$$

## 2.2 Welding and Welded Joints

### 2.2.1 Welding Techniques

Welding is a joining technique where two metal parts (generally of the same material) are heated beyond their melting point and thus fused together as they cool down. Welding can be generalised into two the main categories, namely electric arc welding and friction based welding. In this thesis, the focus will lie on arc welding techniques.

In arc welding, an electric circuit is formed between the welding machine and the parts that are to be joined together. In the transition between the parts and the welding machine and arc is formed. This arc originates from what is called an electrode. Welding electrodes can be made of various metals depending on its intended use. When the electrode is made from tungsten (or other similar alloys), the electrode does not melt at normal welding temperatures (non-consumable welding). In other cases the electrode is made of a similar alloy as in the parts that are to be joined together, so that it melts into the welding pool and acts like a filler material (consumable welding). When welding with a non-consumable electrode filler material has to be added to the weld pool separately. [8]

Generally molten metal reacts to normal atmospheric gasses such as oxygen, leading to rapid oxidation of the welded material thus producing a weld of poor strength and quality. For this reason, shielding gasses are used when welding metals. The purpose of the shielding gasses is to replace the gasses surrounding the molten weld pool and thus producing an environment where there is no oxidation. Shielding gasses can generally be divided into two subgroups, inert and active gasses. When welding with an inert shielding gas, the gas does not influence the welding, it only creating an oxygen-free environment surrounding the molten weld pool. Inert gasses used for welding is often argon (Ar) and helium (He) or a mixture of the two<sup>1</sup>. When using an active shielding gas, the gas affects the welding process in addition to creating an oxygen-free environment around the molten weld pool. For example, when welding with a carbon-dioxide ( $CO_2$ ) and argon mixture, the  $CO_2$  makes the gas slightly conductive thus increasing the welding arc voltage. Generally an active shielding gas is only used when welding carbon steel or steel alloys. Altering the gas types used, the mixture or the ratio of the mixed gasses can also affect the properties and the shape of the finished weld.

Another critical factor when welding is the applied current. Welding can both be done with Alternating Current (AC) and with Direct Current (DC). AC is often used when welding

---

<sup>1</sup> other inert gasses can also be used

materials prone to oxidation, such as aluminum. An important parameter when welding with AC is the frequency of alternation (the change in polarity). When welding with DC the polarity is important (the flow direction of electrons). The energy of the electrons increase as they go through the arc, thus the receiving end of the arc becomes the most heated. Therefore, when welding with a non-consumable electrode the electron flow generally goes from the electrode and down to the base material, thus limiting the chances for exceeding the melting temperature of the electrode. When welding with a consumable electrode the electron flow generally goes from the base material and into the electrode, thus melting it.

When subjecting metal to a substantial amount of heat (near its melting temperature), its material properties and metallurgical structure tends to be altered. The transition between the weld metal and the base material is referred to as the heat-affected zone (HAZ), see figure 2.2. This region refers to the part of the base metal that has been affected by the heat from welding. In many cases, this region can be the origin of defects such as cracks, porosities and/or local entitlements. Therefore the HAZ is often regarded as one of the most critical parts of a weld. [9]

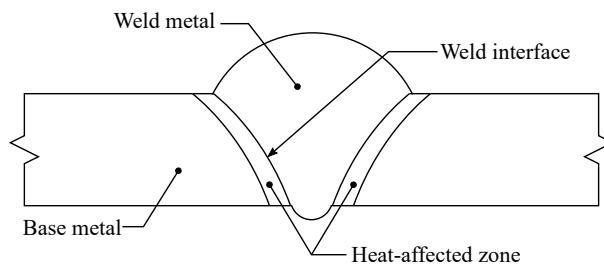


**Figure 2.2:** Heat-affected zone in butt welded plate

There are over a 100 different welding processes, but for this thesis the focus will lie on the two most common for magnesium and magnesium alloys: Gas Metal Arc Welding (GMAW also referred to as Metal Inert Gas welding or MIG for short) and Gas Tungsten Arc Welding (TIG). MIG uses a consumable electrode generally made from an alloy similar to that of the base material. The electrode is fed through the welding gun at a constant rate (which is predetermined by the type of metal welded, its thickness, geometry, etc.) and applied a current. The electrode melts and becomes a filler material to the weld pool. As the name applies, MIG uses an inert shielding gas. When welding with MIG the current can be either AC or DC, but when using DC it is crucial that the polarity is such that the electrons are flowing from the base material and into the electrode, thus melting it. In TIG the welding electrode is made from tungsten and is a non-consumable type electrode. When welding TIG the welding gun generates an arc between the base material and the tungsten electrode which then melts the base material. Filler material has to be added separately to the molten weld pool. TIG can also be used with both AC and DC. When using DC it is important that the electron flow is from the electrode and down into the base material, thus preventing the electrode from melting. MIG and TIG welding are illustrated in figure 2.3. [10]

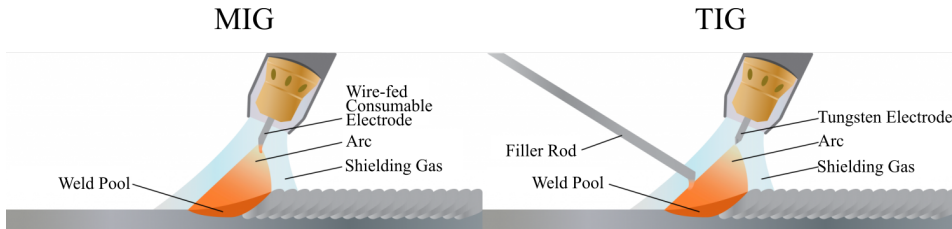


**Figure 2.3:** Illustration of MIG and TIG welding techniques. Graphics From: weldingsupplies-fromioc.com

### 2.2.2 Weld Geometries

As in many forms of joining, the geometry of the welded joint can greatly impact the strength and durability of the finished joint. In arc welding, there are two main welds: butt weld and fillet weld. Butt welding is used when joining two plates which lie in the same plane. Where they can be welded either from one side or both sides. The weld can also either be fully penetrated or non-penetrated, meaning that there is a small area of the cross-section of the two plates that is not fully joined together. A fully penetrated butt welded plate generally provides a stronger joint compared to one that is non-penetrated. In a fillet weld, the two plates that are to be joined together are orientated at an angle relative to each other. The fillet weld can also be either fully penetrated and non-penetrated, depending on the preparatory work done to the joining parts. [11]

Important and critical parts of the weld bead is the weld toe and the weld root, as they both cause stress concentration. In figure 2.4 these two features of the weld bead are shown.

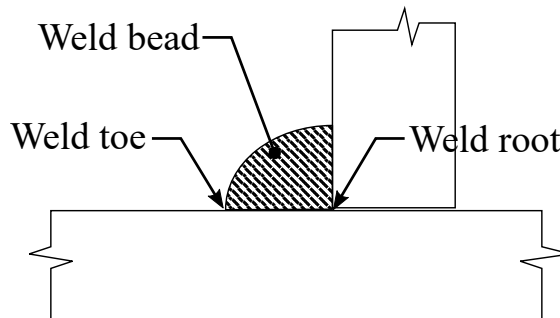


**Figure 2.4:** Important weld geometry terminology

## 2.3 Fracture Mechanics

### 2.3.1 Basics of Fracture Mechanic

The field for fracture mechanics deals with solid materials that suffer failure caused by crack initiation and crack propagation. There are two main approaches to establish a failure criterion for solid materials: crack tip stress field (i.e., the stresses which occurs in front of the crack tip) and energy balance. Most solid materials that are subjected to loading, experience an elastic and a plastic deformation regime. Therefore, fracture mechanical theory it distinguishes between loading in the elastic regime<sup>2</sup> and loading which occurs in the plastic regime. Loading in the elastic regime is called Linear Elastic Fracture Mechanics (LEFM), and loading in the plastic regime is referred to as Elastic-Plastic Fracture Mechanics (EPFM). Figure 2.5 illustrates the fundamental differences between LEFM and EPFM. The cross-hatched region of figure 2.5 portray stresses which can be present in a linear elastic material but not in a elastic-plastic material, because it can not exceed yield ( $\sigma_{yy} \leq \sigma_{YS}$ ) [12].

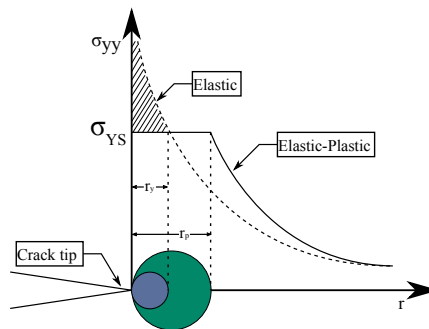


**Figure 2.5:** Difference between LEFM and EPFM in regards to crack tip stress field,  $\theta = 0$

The first approach to estimating the required load to propagate a crack in LEFM is the crack tip stress field. The stresses and displacement of the crack can be evaluated to obtain parameters which in terms can be used to describe the stress field in front of the crack tip. The stresses in front of the crack increase exponentially as we approach the crack tip, and at the crack tip the stresses are unbound and is therefore, regarded as a singularity. The crack tip singularity makes classic approaches to estimating failure strength of solid materials inapplicable. The stresses at the crack tip are limited only by the yield stress of the material or rather the cohesive strength between the atoms. A fundamental part of fracture mechanics is therefore to accept the fact of the crack tip singularity but not directly use it when estimating the failure load. In LEFM the stresses in front of the crack tip can

<sup>2</sup>i.e., loading that corresponds to stresses under the yield strength of the solid material

be described using equation 2.3 (for mode I loading) [13, 14]:

$$\begin{aligned}
 \sigma_{rr} &= \frac{K_I}{\sqrt{2\pi r}} \cos \frac{\theta}{2} \left( 1 + \sin^2 \frac{\theta}{2} \right) + T \cos^2 \theta + O(r^{1/2}) \\
 \sigma_{r\theta} &= \frac{K_I}{\sqrt{2\pi r}} \cos^3 \frac{\theta}{2} + T \sin^2 \theta + O(r^{1/2}) \\
 \sigma_{\theta\theta} &= \frac{k_I}{2\sqrt{2\pi r}} \cos \frac{\theta}{2} \sin \theta + T \sin \theta \cos \theta + O(r^{1/2})
 \end{aligned} \tag{2.3}$$

The stress field in front of the crack has three main attributes: K, T and O.  $K_I$  is called the stress intensity factor. It is depended on the loading type, geometry, and material. It has a unit of stress pr. area squared (generally  $MPa\sqrt{m}$ ). These equations are assuming that the stresses are symmetric around the crack tip. Hence the stress at a given point can be described by the polar coordinates  $r$  and  $\theta$ . Based on equations 2.3, G.R. Irwin proposed that a crack grows as the stress intensity factor reaches a critical value [15]. This value is called fracture toughness ( $K_{Ic}$ ).  $K_{Ic}$  and is a material constant which characterizes a solid material's ability to resist crack extension.

$K_I$  is only valid for mode I loading. Mode I refers to in which direction the crack is loaded. There are three fracture modes (as illustrated by fig. 2.6): mode I (crack opening), mode II (In-plane shear) and mode III (Out-of-plane shear). A mixed mode loading scenario is also possible depending on the crack's orientation, to the loading direction. T-stress is the second non-singular term of the linear elastic stress field. It represents the stresses parallel to the crack. The magnitude of the T-stress contribution can in-term affect the direction of crack growth [13, 16]. O-stresses are other small attributes to the crack stress field. In most cases the crack stress field is considered as K-dominant, meaning that the attributes from T, and O is considered as neglectable [17].

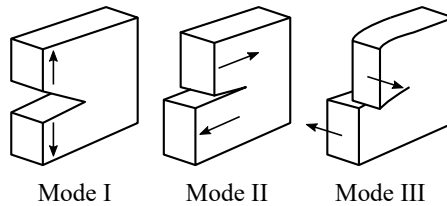


**Figure 2.6:** Fracture modes

The second approach to solid material fracture criterion is by considering the global energy balance of the solid during crack initiation and growth. According to the first law of thermodynamics, when a system goes from a non-equilibrium state to equilibrium, there is a reduction of the stored energy in the system. This is why, by considering the potential energy of a two dimensional crack in an elastic solid, with a crack length,  $a$ . The potential energy pr. unit thickness of the two-dimensional solid can be described by  $\Pi = \Pi(a)$ , where the potential energy is a function of the crack length  $a$ . For a small change in the crack length  $da$ , the decrease of potential energy in the system is  $-d\Pi$ . A.A. Griffith

was the first to apply the thermodynamic law to cracks, and in 1920 proposed that during crack propagation the change in potential energy was absorbed into the surface energy of the two-dimensional structure [18]. He introduced the following energy balance equation shown in equation 2.4. Where  $\Pi$  is the potential energy in addition to strain energy and external forces,  $W_s$  is the work required to create a new surface,  $\gamma_s$  is the surface energy of the material and  $dA$  is the crack area [14].

$$-\frac{d\Pi}{dA} = \frac{dW_s}{dA} = \frac{\pi\sigma^2 a}{E} = 2\gamma_s \quad (2.4)$$

By solving equation 2.4 for fracture stress, it gives equation 2.5 ( $E$  is total energy). The major drawback of Griffith's approach is that it is only applicable for ideally brittle solids. Hence, later there are proposed modified Griffith equations based on experimental data.

$$\sigma_f = \left( \frac{2E\gamma_s}{\pi a} \right)^{\frac{1}{2}} \quad (2.5)$$

Irwin proposed the energy release rate  $G$ , which is defined as the decrease in potential energy pr. unit crack expansion under a constant load. He also suggested that crack propagation occurs when the energy release rate meets a critical value of  $G_c$  [14]:

$$G = G_c = \frac{d\Pi}{da} = \frac{\pi\sigma^2 a}{E} \quad (2.6)$$

The relationship between the critical strain energy release rate and the fracture toughness can be found by combining equation 2.3 (for  $\theta = 0$  and K-dominance) and 2.5. This relationship is illustrated by equation 2.7, where also the relationship for a plane strain scenario is shown. The difference between the plane strain and the plain stress equation is the attribute from the *Poisson ratio* of the solid.

$$\begin{aligned} \text{Plane stress, } K_{IC} &= \sqrt{EG_c} \\ \text{Plane strain, } K_{IC} &= \sqrt{EG_c(1 - \nu^2)} \end{aligned} \quad (2.7)$$

The size of the cracked solid can affect the estimation of its critical load, because the plastic zone at the crack tip must be relatively small compared to the thickness of the cracked solid. This is so that the specimen thickness is adequate to ensure a plane strain condition ( $\sigma_{zz} \neq 0, \varepsilon_{zz} = 0$ ) at the intersection between plastic and elastic loading zones. When the plastic zone has grown to make up a considerable amount of the specimen thickness, the outer edges of the zone change to a plain stress condition ( $\sigma_{zz} = 0, \varepsilon_{zz} \neq 0$ ), but it still experiences plane strain at the center of the plastic zone. With further plastic deformation, the amount of triaxial stress at the crack tip declines. A lower value of triaxial stress generally results in a higher fracture toughness, thus influencing the critical value of crack propagation [12]. This is why generally a thin specimen has a higher fracture toughness than a thick one. As a result of this phenomenon, the American Society for Testing and Materials has proposed a standard for specimen size were  $K_{Ic}$  is valid, and LEFM applies. These specimen guidelines are illustrated by equation 2.8, where  $a$  is the crack length,  $B$  is the specimen thickness and  $W$  is the specimen width [12].

$$a, B, (W - a) \geq 2.5 \left( \frac{K_I}{\sigma_{YS}} \right)^2 \quad (2.8)$$

### 2.3.2 Cracks versus Notches

The topic of cracked or fracture solids is a well-developed part of the fracture mechanics field, compared to the relatively new study of notches solids. In regards to fracture mechanics, notches and cracks both result in stress concentration at their root and thus are a critical part of a structure. Therefore in some cases, the methods for determining the critical loads for cracked solids as described earlier are applicable for notches as well. Notches are generally portrayed as cracks, with a crack length  $a$ , an opening angle greater than zero ( $2\alpha > 0$ ) and with a blunt (notch tip radius  $\rho$ ) or sharp tip (see figure 2.7).

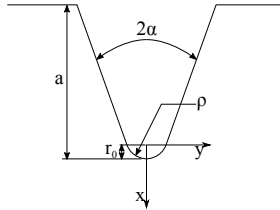


**Figure 2.7:** Blunt v-notch, with common designations

In sharp V-shaped notches, the stresses at its tip result in the same type of stress singularity as in cracked solids. V-shape notches with a blunt notch tip can also generate stresses that surpass that of the ultimate strength of a material. These stress concentrations and singularities limit the use of traditional approaches to calculating the failure load of a notched solid in the same way as with cracked solids. An important injunction in developing generalized fracture criterion for v-notched solid bodies is that the stress intensity factor varies with the notch opening angle  $2\alpha$ , thus resulting in that the unit of stress intensity also varies with  $2\alpha$ . Notches also experience the effect of loading direction as with cracks. Thus, the fracture modes described earlier still applies. The stress concentration at the notch tip (i.e., close to) can be expressed with equation 2.9 for sharp notches. To calculate the stress intensity of blunt notches equation 2.11 must be applied. Where  $\tilde{\omega}$  and  $\mu$  are constants dependent of the notch opening angle and is found in the literature [19].  $r_0$  in equation 2.12 is a parameter which compensates for the blunt notch, and is based on the notch opening angle and the notch tip radius  $\rho$  [20]. The  $\lambda_I$  and  $\lambda_{II}$  are functions of the notch opening angle and is derived by equation 2.10 (see fig. 2.8), they are called stress singularity exponents. From equation 2.9 we can see that the unit for the stress intensity factor varies with the notch opening angle. As a result, a stress intensity factor from a cracked solid or from a notch with a different  $2\alpha$  can not be directly compared. In other words, the notch stress intensity factor (NSIF) is geometry dependent.

$$\begin{aligned}
 K_I^\lambda &= \lim_{\theta=0} \lim_{r \rightarrow 0} \left[ \sqrt{2\pi r}^{1-\lambda_I} \sigma_{\theta\theta}(r, \theta) \right] \\
 K_{II}^\lambda &= \lim_{\theta=0} \lim_{r \rightarrow 0} \left[ \sqrt{2\pi r}^{1-\lambda_{II}} \tau_{r\theta}(r, \theta) \right]
 \end{aligned} \tag{2.9}$$

From figure 2.8 which is a plot of the notch opening angle versus  $\lambda_I$  and  $\lambda_{II}$  (eq. 2.10), it is apparent that the stress concentration factor for *mode II* loading cannot be calculated of  $2\alpha > 100^\circ$  using equation 2.9 [21]. Notches with a larger opening angle can be solved with the help of the finite element method (FEM). A two-dimensional simplification of the notched region and the use of elasticity theory is most appropriate when solving of such problems with the aid of FEM[22].

$$\begin{aligned}
 (1 - \lambda_I) \sin 2\alpha + \sin 2(1 - \lambda_I)\alpha &= 0 \\
 (1 - \lambda_{II}) \sin 2\alpha + \sin 2(1 - \lambda_{II})\alpha &= 0
 \end{aligned} \tag{2.10}$$

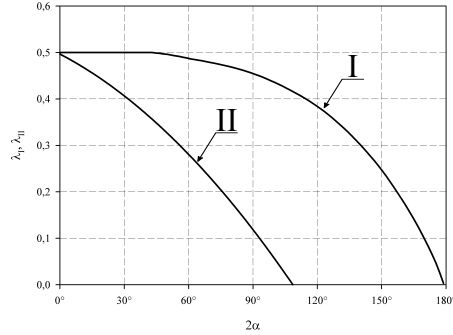


**Figure 2.8:** Plot of equation 2.10 for mode I and mode II loading,  $\lambda_I$  and  $\lambda_{II}$  as a function of notch opening angle  $2\alpha$ .

Determination of the NSIF using FEM can be done through different approaches. Some of the methods find the NSIF using direct methods, which provides the NSIF value directly from the stress field around the notch tip; asymptotic methods, where stress distributions near the stress singularities are compared both analytically and numerically. Energy based methods are also used, they are based on energy integrals independent of the integration path such as J-integral. [22]

$$\begin{aligned}
 K_{\rho,I}^V &= \sqrt{2\pi r}^{1-\lambda_1} \frac{(\sigma_\theta)_{\theta=0}}{1 + \tilde{\omega}_1 \left(\frac{r}{r_0}\right)^{\mu_1 - \lambda_1}} \\
 K_{\rho,II}^V &= \sqrt{2\pi r}^{1-\lambda_2} \frac{(\tau_{r\theta})_{\theta=0}}{1 + \tilde{\omega}_2 \left(\frac{r}{r_0}\right)^{\mu_2 - \lambda_2}}
 \end{aligned} \tag{2.11}$$

$$r_0 = \frac{\left(1 - \frac{2\alpha}{\pi}\right) \cdot \rho}{\left(2 - \frac{2\alpha}{\pi}\right)} \quad (2.12)$$

Another way of describing the effect of introducing a notch to a solid body is through the use of a stress concentration factor. It describes the relationship between the maximum stress caused by the notch and the nominal stress in the solid (see eq. 2.13). An advantage with the stress concentrations factor is that it is independent of loading direction (relative to the notch) and geometry. The stress concentration factor is not applicable for crack and notches with a sharp tip and a small opening angle, because of the crack tip singularity it might cause.

$$K_t = \frac{\sigma_{max}}{\sigma_{nom.}} \quad (2.13)$$

### 2.3.3 Strain Energy Density

The use of such traditional approaches as crack tip stress field and global energy in strength assessment of cracks and notched solids are not always applicable. Especially under mixed-mode loading (e.g. *mode I + mode II*), and in the case of notched solid the limitations of the traditional approaches are apparent. G. C. Sih found it problematic that the classic fracture criterion only applied to idealized specimens under certain loading conditions, this in turn, imposed restrictions on the geometry of the imperfection (i.e., cracks and notches) that may be evaluated. Also, the use of the fracture criterion  $G_{Ic}$  and  $K_{Ic}$  do not account for the blunting of the crack tip due to plastic deformation, under cyclic loading. Therefore in 1973 G.C. Shi proposed a new energy-based fracture criterion called strain energy density (SED)[23]. SED was to be a geometry-independent and a mixed-mode applicable fracture strength criterion. The fundamental definition of strain energy density  $dW/dV$ , is the quantity of strain energy contained in a unit volume of a solid at a given instance. SED has proven to be a useful criterion, and have been used to solve two- and three-dimensional crack problems; notched problems; dynamic crack problems; fatigue crack growth, etc.[24]

$$\frac{dW}{dV} = \int_0^{\varepsilon_{ij}} \sigma_{ij} d\varepsilon_{ij} + f(\Delta T, \Delta C) \quad (2.14)$$

SED may be seen as an assembly built up out of small blocks which together makes up a solid. Each of the blocks is consisting of a specific volume and with the ability to store a finite amount of energy at a given instance. One way of calculating SED is through the use of equation 2.14. Where  $\varepsilon_{ij}$  and  $\sigma_{ij}$  are strain and stress components, and  $\Delta T$  and  $\Delta C$  the change in temperature and moisture. For linear elastic materials, the SED can be calculated using equation 2.15.

$$\frac{dW}{dV} = \frac{1}{2E}(\sigma_x^2 + \sigma_y^2 + \sigma_z^2) - \frac{\nu}{E}(\sigma_x\sigma_y + \sigma_y\sigma_z + \sigma_z\sigma_x) + \frac{1}{2\mu}(\tau_{xy}^2 + \tau_{yz}^2 + \tau_{zx}^2) \quad (2.15)$$

Where  $\sigma_x, \sigma_y, \sigma_z, \tau_{xy}, \tau_{yz}$  and  $\tau_{zx}$  are stress components,  $E$  is the modulus of elasticity,  $\nu$  is the Poisson ratio and  $\mu$  is the elastic shear modulus (often referred to as "G-modulus") [24].

ASED as a fracture criterion on more general geometries such as cracks and notches was first possible through the work of Prof. P. Lazzarin (and others). The concept of *Local strain energy density approach* is a fracture criterion based on the average ASED ( $\bar{W}$ ) in a defined control volume. This approach corresponds to Neuber's concept of an *elementary material volume* used for stress averaging [3, 25]. It is elaborated for sharp and blunt v-notches as well as for cracks and other imperfection geometries. In addition, the application has been extensively tested for tensile loading (mode I) and also for some cases of mixed-mode lading [26, 27, 28]. Average ASED has also been used as a fatigue strength parameter for welded steel and aluminum joints [4].

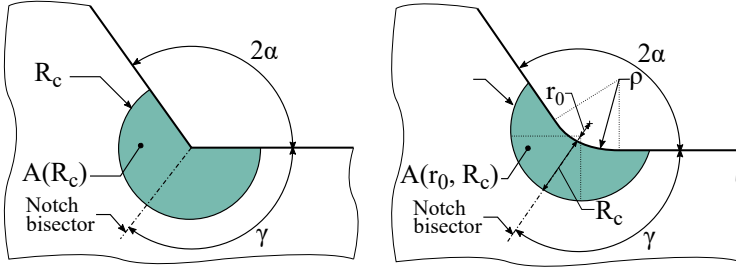


**Figure 2.9:** Control radius on sharp V-notch and a blunt tip V-notch

As stated earlier, the ASED is calculated in a volume defined by a control radius, which is called  $R_c$ .  $R_c$  for a blunt V-notch or a crack is applied at the notch/crack tip as illustrated in figure 2.9. Under plane strain condition and with a static load  $R_c$  may be calculated using equation 2.16. The control radius is based out of material constants such as the Poisson ratio  $\nu$ , fracture toughness  $K_{Ic}$  and the ultimate tensile strength  $\sigma_U$ , which in-turn makes the control radius geometry independent. If the notch tip is blunt, the control radius center point has to be shifted by a factor of  $r_0$  from the edge of the blunt notch tip as illustrated by figure 2.9 [20].

$$R_c = \frac{(1 + \nu)(5 - 8\nu)}{4\pi} \left( \frac{K_{Ic}}{\sigma_U} \right)^2 \quad (2.16)$$

$\bar{W}$  can be calculated using equation 2.17 and 2.18, which is a function of the defined control radius  $R_0$ . The notch opening angle ( $2\alpha$ ) dependent values of  $I_1(\gamma)$ ,  $I_2(\gamma)$ ,  $\lambda_1$  and  $\lambda_2$  can be found in appendix A. As apparent by 2.8, at notch opening angles ( $2\alpha > \sim 100^\circ$ ) the contribution from *mode II* loading can be neglected since the value of  $(1 - \lambda_2)$  will be less than zero.

$$\bar{W}(R_c) = \frac{e_1(\gamma)}{E} \cdot \left( \frac{K_I}{R_c^{(1-\lambda_1)}} \right)^2 + \frac{e_2(\gamma)}{E} \cdot \left( \frac{K_{II}}{R_c^{(1-\lambda_2)}} \right)^2 \quad (2.17)$$

$$e_1(\gamma) = \frac{I_1(\gamma)}{4\lambda_1\gamma} \quad e_2(\gamma) = \frac{I_2(\gamma)}{4\lambda_2\gamma} \quad (2.18)$$

P. Lazzarin and R. Zambardi proposed a fracture criterion based on the ASED called  $W_c$  [29].  $W_c$  can be calculated with equation 2.19, which is based on the ultimate strength ( $\sigma_U$ ) and Young's modulus ( $E$ ) of the material. They proposed that failure will occur when the average value of deformation energy reaches the critical SED ( $\bar{W} \leq W_c$ ).

$$W_c = \frac{\sigma_U^2}{2E} \quad (2.19)$$

Since the control radius and the failure criterion for SED are based on material constants, ASED can be regarded as geometry independent. A feature which is useful when assessing, for example, fatigue failure. Figure 2.10 shows the result of applying ASED theory to about 900 steel alloy specimens of different geometries under cyclic loading conditions [30]. In traditional approaches to fatigue life estimations there would be a need to construct individual plots for different geometries and mean stresses which then again could not be directly compared, and as is apparent by figure 2.10 this would no longer be the case when applying ASED as a fatigue criterion. When using ASED as a criterion in fatigue life assessment, the control radius is calculated by equation 2.20. This equation is based on the resulting NSIF in a V-notched specimen ( $\Delta K_{IA}$ ), loaded at the stress range ( $\Delta\sigma_A$ ) at the fatigue limit ( $N_a = 5 \cdot 10^6$  cycles) of a welded specimen where the welds are ground smooth (i.e. an un-notched specimen). [3]

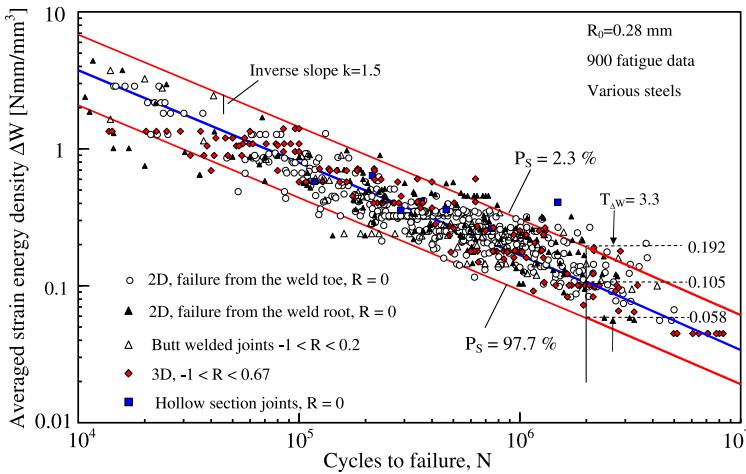


**Figure 2.10:** Plot of  $\Delta W$  vs.  $N_f$  for different steel geometries. Image from paper: Rapid calculations of notch stress intensity factors based on averaged strain energy density from coarse meshes: Theoretical bases and applications by P. Lazzarin *et al.* (2010) [30]

$$R_c = \left( \sqrt{2}e_1 \cdot \frac{\Delta K_{IA}}{\Delta\sigma_A} \right)^{\frac{1}{1-\lambda_1}} \quad (2.20)$$

ASED has been proven to only slightly be influenced by the mesh size and the number of elements present within the control volume when applied to notches and cracks. This is beneficially in Finite Element Analysis (FEA) of large structures as the reduced number of elements needed for an accurate result will again reduce the necessary computer resources needed. The variation range in ASED compared to the number of elements used in the FEA has been found to be around 4.0% to 6.4% for full circles (often used for cracks) and from 2.0% to 4.7% for semicircles (often used for notches) [30].

## 2.4 Magnesium and AZ31 Magnesium Alloy

Traditionally, the primary use of magnesium has been as an alloying additive to other metals (i.e. some aluminum alloys), due to the favorable metallurgical properties it provides [31]. Pure magnesium is a relatively soft material with poor mechanical properties and is, therefore, uncommon to be used in structural components. Magnesium alloys, on the other hand, are often the materials of choice for lightweight (low density  $\approx 1.8 \text{ kg/dm}^3$ ) and high strength components. It also has favourable properties when it comes to casting. Common designations for magnesium alloys are listed in table 2.2. In the designation of a magnesium alloy the alloying element(s) is followed by a serial number which describes the percentage of alloying material (rounded up to the nearest whole number), i.e. in AZ61 magnesium alloy, the main alloys are Aluminum - 6% and Zinc - 1%. Joining of magnesium alloys can be done with most conventional methods such as welding, bolting, adhesive bonding, etc. Welding of magnesium alloys is almost exclusively carried out with TIG or MIG.

**Table 2.2:** Magnesium alloy designations [32]

A	aluminum	M	manganese
C	copper	Q	silver
E	rare earth metals	S	silicone
G	magnesium	T	tin
H	thorium	W	yttrium
K	zirconium	Z	zinc
L	lithium		

AZ31 magnesium is, as the name (serial number) implies, a commercial grade magnesium alloy where the main alloying elements are aluminum and zinc. A detailed description of the chemical composition of AZ31 magnesium is found in table 2.3. The AZ31 alloy is a moderate-strength, general-purpose magnesium alloy, often used in the production of ladders and hand luggage. It comes in both rolled sheets form and as extrusions. It is especially desirable for extrusion, due to relative high extrusion speed compared to other magnesium alloys (i.e. AZ61A and AZ80A magnesium alloy). Material properties of AZ31 are listed in table 2.4 (for detailed material properties see table B.1 in appendix B). [32]

**Table 2.3:** Chemical composition of AZ31 magnesium alloy [33]

Material	Al	Si	Fe	Cu	Mn	Ni	Zn	Mg
Magnesium AZ31 (ISO.MgAl3Zn1)	2.850%	0.050%	0.003%	0.001%	0.290%	0.001%	0.950%	95.855%

**Table 2.4:** AZ31 magnesium alloy material properties. <sup>1</sup>[34], <sup>2</sup> [35]

Parameter	
Density <sup>1</sup>	1.77 g/cm <sup>3</sup>
Young's modulus, $E^1$	43 GPa
Poisson ratio, $\nu^1$	0.35
Tensile strength, <sup>2</sup> $\sigma_u$	224 MPa
Monotonic yield strength, <sup>2</sup> $\sigma_{p0,2}$	197 MPa

# Chapter 3

## Literature review

When conducting new research in a field of study, it is of great importance to have knowledge of the previous work done by others concerning the same topic. As it comes to fatigue lifetime estimation of welded AZ31 magnesium alloy joints with the aid of ASSED theory, there have not been conducted any research prior to this thesis. There have, on the other hand been conducted numerous studies on fatigue lifetime estimation of AZ31 magnesium using other known techniques. Also in the field of ASSED, there have been performed fatigue lifetime estimations on welded joints of materials with similar material properties as AZ31 magnesium alloy. Hence, in this literature review, the focus will lie on understanding other approaches to fatigue life estimations on AZ31 magnesium alloy, as well as familiarizing with the use of ASSED theory to predict fatigue life of similar materials. The papers that are reviewed were selected on the grounds of their relevance to the topic of this thesis.

### 3.1 AZ31 Magnesium Alloy

#### 3.1.1 Fatigue of Welded Magnesium Alloy Joints

Paper by M. Tsujikawa *et.al.* [36]. The main scope of the paper was to investigate the factors which govern the fatigue strength of welded joints made of commercial grade magnesium alloys. Investigations were carried out experimentally on both extruded and rolled AZ31 and AZ61 magnesium alloy. The welding processes used were TIG and Friction Stir Welding (FSW) (both fully penetrated welds, welded from one side, i.e. non-symmetrical weld). Joint efficiencies for fatigue and static strength were measured ( $\sigma_{joint} / \sigma_{base\ metal}$ ); Scanning Electron Microscopy (SEM) was used to observe initial points of fatigue crack initiation and crack propagation.

Specimens were made of to plates<sup>1</sup> of the same alloy welded together, forming a butt joint. For the TIG welded specimens, filler material of the same alloy was used. After welding, the specimens were cut so that the weld line was across the tensile axis at the centre. Specimens were made from both parallel and normal to rolling/extrusion direction. All specimens were inspected with X-ray radiography; only sound specimens were used for testing. The total pass rate for TIG-welded specimens were 89%, no FSW specimens failed X-ray inspection. The microstructure for the weld metal, HAZ and base metal for both welding methods are shown in figure 3.1. The fatigue testing was conducted in air at room temperature;  $R = 0.1$ ; the pulse shape was sinusoidal with a frequency of 10 Hz.

---

<sup>1</sup>plate thickness for AZ31 was 2 mm and was 4mm for AZ61

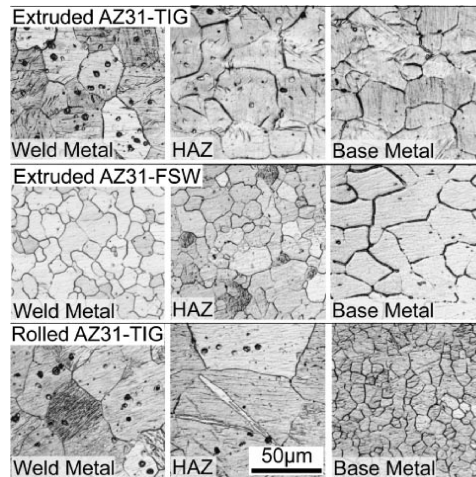


**Figure 3.1:** Microstructures of welded joints of AZ31 [36]

Reported results from the fatigue testing were presented graphically in the form of S-N curves (stress versus number of cycles to failure). These indicate that the slope of the S-N curves for welded joints was more inclined than those of specimens made from pure base metal (non-welded). That is, an increase in load decreases the fatigue life of a welded specimen more compared to one made from just the base material. Fatigue strength of the welded specimens was found to be lower than that of non-welded specimens, despite the increased thickness at the weld. The joint efficiencies were found to be over 90% for static failure of TIG welded joint (both AZ31 and AZ61) and 89% and 78% for AZ31 and AZ61 joints welded with FSW. Efficiency of fatigue strength was around 60%, except for joints of extruded AZ31. They had a joint efficiency around 80%, regardless of welding method.

SEM inspections of the fatigue fracture surfaces of the TIG welded joints shows that the fatigue crack always propagated from the weld toe of the bead line. Moreover, it was observed that 83% of the cracks initiated from the backside weld toe. The crack growth path was found to be vertical to the loading axis. The points of crack initiation are at stress concentration points in the weld. Which were found to be most severe in the heat-affected zone, where large grains were present. The fracture surfaces occurred in weld metal which was found to consist of equiaxed grains which have a random crystal orientation. Microscopy of crack propagation during fatigue of welded magnesium joints indicate that the fatigue crack growth paths are highly dependent of crystallographic orientation. [36]

### 3.1.2 Critical distance approach for the fatigue strength assessment of magnesium welded joints in contrast with Neuber's effective stress method

Paper by Ö, Karakaş [35]. The scope of this paper was to apply critical distance method to evaluate fatigue behaviour of welded joints made from AZ31 magnesium alloy, and then to compare the results to fatigue life estimations using Neuber's stress averaging method. The geometries considered were fully penetrated butt welded plate, non-penetrated butt welded plate and plate with a welded transverse stiffener. Evaluated data were found experimentally as the three geometries were subjected to three different type of loads, namely:  $R=-1$ ,  $R=0$  and  $R=0.5$ . Stress distributions for each geometry were acquired with the aid of finite element analysis (FEA).

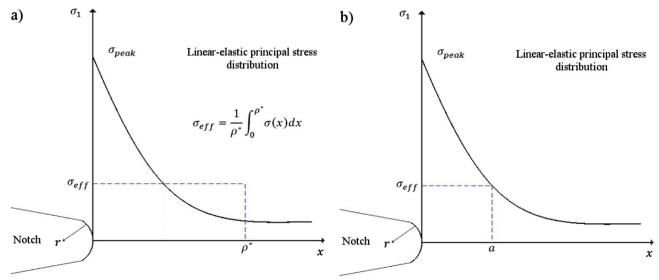


**Figure 3.2:** Representation of the stress averaging method (a) and the critical distance method (b). [35]

The aim of both Neuber's stress averaging and critical distance method is to calculate an effective stress at the notch tip of a geometry subjected to stresses, and thus using it as a fatigue parameter in an S-N plot. This effective stress is determined by the stress distribution close to the notch tip. The effective stress can then be defined as a scale value, which then corresponds to a designed stress field in the notch ligament. When using Neuber's method this value is found by averaging the stress over a line starting from the notch tip with the length  $\rho^*$ . Using the critical distance method, the effective stress is considered to be equal to the stress calculated with a distance  $a$  from the notch tip. Both these approaches result in the same effective stress. A graphic representation of the difference in Neuber's and critical distance methods are illustrated by figure 3.2.

Both the microstructural length  $\rho^*$  and the critical length  $a$  are based on material properties. Hence, there have been proven to be a relationship between the two parameters of  $a = \rho^* / 4$ . These parameters are found by evaluating experimental fatigue data in FEA. Calculations in the paper were performed for both reference notch radii  $r_{ref} = 1 \text{ mm}$  and  $r_{ref} = 0.5 \text{ mm}$ , which was suggested for the notch stress concept.

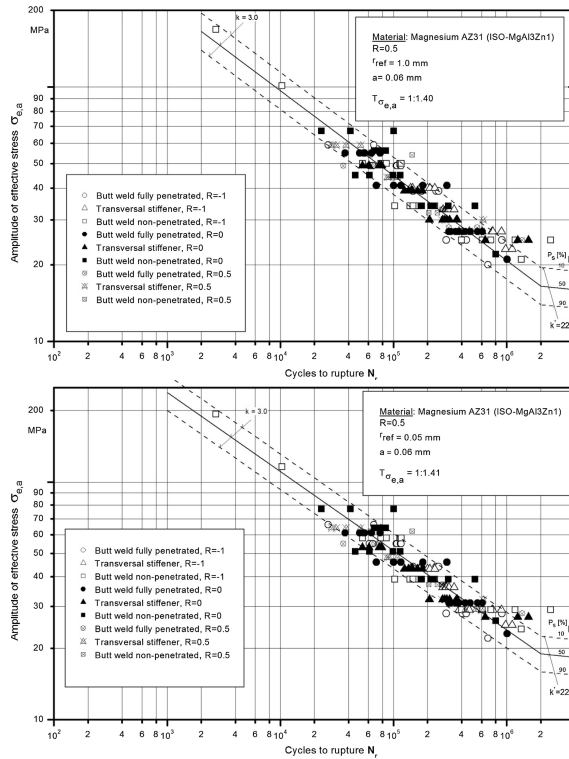


**Figure 3.3:** Resulting S-N curves using the critical distance method for both radii considered. [35]

The three stress ratios,  $R=-1$ ,  $R=0$ , and  $R=0.5$  were all converted to one stress ratio of  $R=0.5$ , using a Haigh diagram for mean stress conversion. The acquired data analyzed returned a critical distance of  $a = 0.06 \text{ mm}$  versus the previous determined microstructural length of  $\rho^* = 0.12 \text{ mm}$ . They found that the critical radius method results in a narrower scatter band compared to scatter bands of traditional S-N curves. By applying both the critical distance method and Neuber’s stress averaging method it was found to reduce the scatter further. The resulting scatter is at about  $T_\sigma = 1 : 1.50$ , which the paper concludes as an indicator that the method is acceptable. This notable reduction in scatter is an indicator that critical distance method is a viable method for predicting the fatigue life of welded AZ31 magnesium alloy[35].

**Table 3.1:** Scatter values of all determined S-N curves [35]

Method	$1 : T_\sigma$	
	$r_{ref} = 1 \text{ mm}$	$r_{ref} = 0.05 \text{ mm}$
Notch stress	1.76	1.90
Stress averaging ( $\rho^* = 0.12 \text{ mm}$ )	1.50	1.45
Critical distance ( $a = 0.12 \text{ mm}$ )	1.40	1.41

## 3.2 Local Strain Energy Density

### 3.2.1 Fatigue strength of steel and aluminum welded joints based on generalised stress intensity factors and local strain energy values

Paper by P. Livieri and P. Lazzarin [4]. P. Livieri and P. Lazzarin found that the use of Notch Stress Intensity Factor (NSIF) approaches to predict the fatigue life of welded joints were problematic. From a theoretical point of view, methods based on NSIF are not applicable for welded joints with a flank angle that differs much from 135° (regular angle for fillet welds). Simply because of the unit of the NSIF [ $MPa m^\beta$ ], where  $\beta = 1 - \lambda$ , a parameter which again is dependent of the flank angle (notch opening angle,  $2\alpha$ ) of the weld. Thus the NISF from a joint with one flank angle would not be comparable with one with another flank angle. In this paper, they have re-analyzed fatigue data based on NSIF as a fatigue criterion. The data was obtained from the literature, and re-analyzed using local strain energy density theory. A fatigue parameter which is believed to be independent of notch geometry and loading mode. ASED was used over an in-closed volume defined by a critical radius surrounding the weld toe or root (see figure 3.4).

As the data that was re-analyzed in this paper was presented in the form of NSIF range ( $\Delta K$ ), application of ASED range ( $\Delta \bar{W}$ ) as a new criterion was obtained through the use of an analytical approach. As all of the evaluated cases had plain strain conditions with mode I and/or mode II conditions in the highly stressed regions, the resultant  $\Delta \bar{W}$  was calculated using equation 2.17. Parameters for the analytical approach was found by evaluating the notch opening angle for each respective geometry (i.e. the angle of the weld bead), then calculating the appropriate values for  $e_1$ ,  $e_2$ ,  $\lambda_1$  and  $\lambda_2$ .

Appropriate control radius  $R_c$  for both steel and aluminum specimens were acquired through the use of equation 2.20. Using this equation, the paper took into account the experimental value for the range NSIF at 5 million cycles related to a non-load carrying transverse fillet weld, with a notch opening angle of  $2\alpha = 135^\circ$  at the weld.

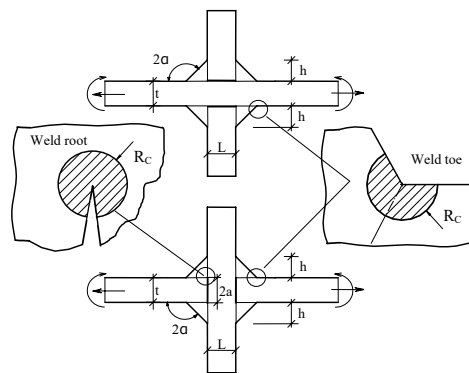


**Figure 3.4:** Geometrical parameters and critical volume (area) at the weld toe and root. [4]

The reanalysis dealt with about 750 specimens in total, both made from various steel and aluminum alloys. The analyzed specimens had plate thicknesses ranging from 6 mm to 100 mm and notch opening angles ranging from  $110^\circ$  to  $150^\circ$  as well as cracked specimens (weld root). The calculated control radii that were calculated and used in this paper were 0.28 mm for steel and 0.12 mm for aluminum, respectively.

The resulting strain energy-based fatigue strengths of the welded steel and aluminum joints are as presented in figure 3.5, which are plots of  $\Delta\bar{W}$  versus number of cycles to failure ( $N_f$ ). The resulting  $\Delta\bar{W}$  was calculated with the assumption that the tested specimens were under full plain strain condition so that material followed linear elastic law. This result shows that by applying a prediction band at 2.3% and 97.7% probability, the resulting scatter band parameter for both steel and aluminum are quite similar.

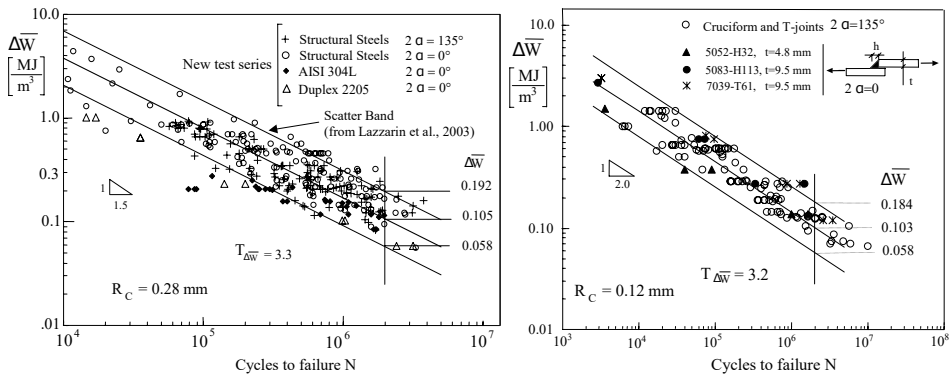


**Figure 3.5:** Strain energy-based scatter band summarizing fatigue strength of welded steel and aluminum joints. [4]

When comparing the the resulting  $\Delta\bar{W} - N_f$  plots for both materials, it indicates that by considering a critical radius of 0.28 mm for steel and 0.12 mm for aluminum the resulting mean value of  $\Delta\bar{W}$  at  $2 \cdot 10^6$  cycles are very close ( $0.105 \text{ } Nmm/mm^3$  against  $0.103 \text{ } Nmm/mm^3$ ) as can be seen from figure 3.6, which is a composition plot of the two. At  $2 \cdot 10^6$  the scatter band parameter is  $T_{\Delta\bar{W}}=3.3$ . When converted over to the stress based scatter parameter  $T_\sigma$  with 10% - 90% probability bands, the scatter parameter becomes  $T_\sigma = \sqrt{3.3} / 1.21 = 1.50$ , which is an exact match for the normalised S-N scatter band's for welded steel. The similarities between steel and aluminum at  $N_f = 2 \cdot 10^6$  are thought to be on the basis of that the two materials have different Young's modulus and critical radius, which somehow cancelled each other out at high cycle fatigue. [4]

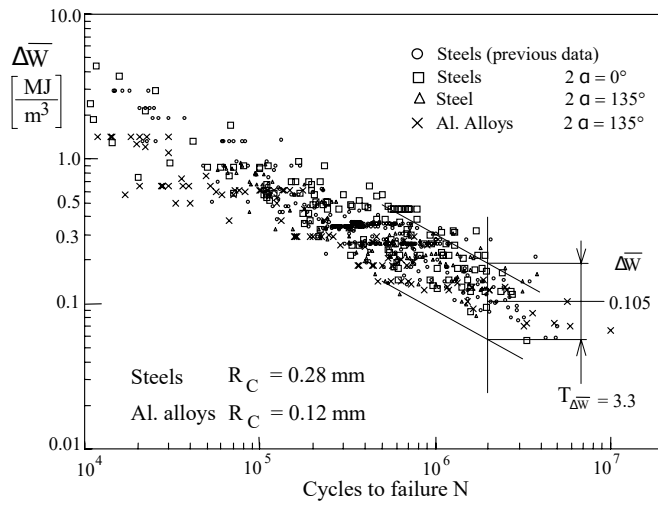


**Figure 3.6:** Strain energy-based scatter bands summarizing about 750 fatigue data of welded joints made of steel and aluminum subjected to tension and bending loads. [4]



# Chapter 4

## Methodology

### 4.1 Experimental Procedure

As previously stated, experimental data and experimental investigation on the fatigue properties of welded AZ31 magnesium alloy joints is conducted by and supplied by Özler Karakaş. Hence, this part of the method chapter is based on information given by Karakaş and material published by him and others concerning this subject [33, 34, 35, 37, 38, 39].

The specimens produced for the experimental investigation were all made of the same magnesium alloy AZ31 (ISO-MgAl3Zn1)<sup>1</sup> in the form of rolled sheets, with a thickness of  $t = 5.3$  mm respectively. The selected welded geometries used are shown in figure 4.2. They are as follows: a fully penetrated butt welded plate; a non-penetrated butt welded plate; plate with a welded transverse stiffener. These three geometries are selected since they all represent specific real-life and critical welding forms which may influence the fatigue life of a welded joint. The number of specimens used in the experimental investigation is specified by table 4.1.

MIG welding was used to manufacture the fully penetrated butt welds and to weld the transverse stiffener to its plate. For the case of the non-penetrated butt welded specimens, TIG welding was used. The filler material was of a commercial AZ61A magnesium alloy with a diameter of  $1.2$  mm. The welding was done in two passes. Both the butt welded geometries were welded from both sides, creating a "symmetric" weld. The parts for the plate with welded transverse stiffener were pre-heated before welding, to  $100^{\circ}C$  for the first pass and to  $120^{\circ}C$  for the second pass. This was done to lessen the effect of shrinkage stresses and distortion which may occur when welding one part to another. The specimens received no post-treatment and were tested "as-is". A detailed description of the welding parameters and process used for each specimen geometry are shown in table 4.2 through 4.4.

**Table 4.1:** Tested specimens

Geometry	Loading ratio		
	$R = -1$	$R = 0$	$R = 0.5$
Fully penetrated butt welded plate	24	23	9
Non-penetrated butt welded plate	28	30	8
Plate with welded transverse stiffener	32	28	15

<sup>1</sup>for chemical compositions and material properties see table 2.3 and B.1

**Table 4.2:** Process-specific parameters and procedures of MIG “Triggered Short Arc” for the fully penetrated butt weled plates [35]

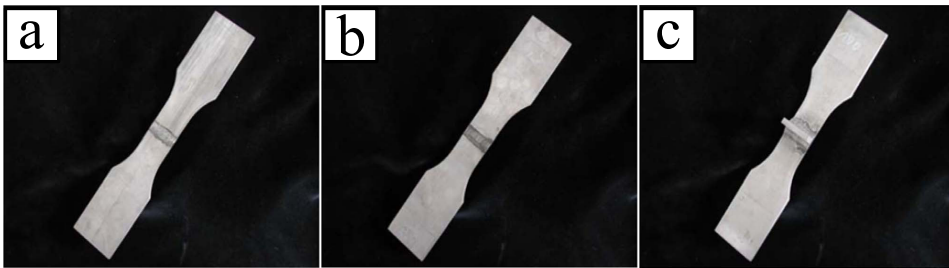
Parameter	Unit	1st pass	2nd pass
Filler material	[-]	AZ 61 A	AZ 61 A
Wire diameter	[mm]	1.6	1.6
Welding speed	[cm/min]	75	104
Wire speed	[m/min]	6.00	8.00
Target voltage (mean)	[V]	17.78	19.07
Ground current before short	[A]	20.53	23.04
Time delay before pulse	[ms]	4.01	4.00
Ground current before pulse	[A]	24.06	26.00
Pulse time	[ms]	11.64	12.55
Pulse current	[A]	262.41	321.71
After-pulse time	[ms]	3.00	3.00
After-pulse current	[A]	29.00	30.00
Argon flow	[l/min]	11-12	11-12
Preheating temperature	[°C]	-	-

**Table 4.3:** Process-specific parameters and procedures of TIG for the non-penetrated butt welded plates [35]

Parameter	Unit	1st pass	2nd pass
Filler material	[-]	AZ 61 A	AZ 61 A
Wire diameter	[mm]	1.6	1.6
Welding speed	[cm/min]	30	30
Wire feed speed	[m/min]	1.3	1.3
Voltage	[V]	16	16
Current	[A]	135	135
Current/Polarity	[-]	sine	sine
Puls rate	[Hz]	80	80
Argon Flow	[l/min]	10	10
Preheating temperature	[°C]	-	-

**Table 4.4:** Process-specific parameters and procedures of MIG “Triggered Short Arc” for the plates with welded transverse stiffener [35]

Parameter	Unit	1st pass	2nd pass
Filler material	[-]	AZ 61 A	AZ 61 A
Wire diameter	[mm]	1.6	1.6
Welding speed	[cm/min]	40	40
Wire speed	[m/min]	6.70	6.70
Target voltage (mean)	[V]	18.60	18.60
Ground current before short	[A]	22.0	22.0
Time delay before pulse	[ms]	4.0	4.0
Ground current before pulse	[A]	26.0	26.0
Pulse time	[ms]	10.0	10.0
Pulse current	[A]	312.0	312.0
After-pulse time	[ms]	3.00	3.00
After-pulse current	[A]	30.0	30.0
Argon flow	[l/min]	11-12	11-12
Preheating temperature	[°C]	100	120

**Figure 4.1:** Picture of welded experimental specimens. a) Fully penetrated butt welded plate , b) non-penetrated butt welded plate and c) Plate with welded transverse stiffener. Image courtesy of Özler Karakaş [35]

The finished welded specimens are shown in figure 4.1. All completed specimens had their critical features measured and recorded as to aid the making of an accurate FEM model using the mean value of the measurements. Also, the micro radii at the notch tip were measured using a roughness measurement unit. In addition, the hardness distributing across the weld seam for the fully penetrated weld and the non-penetrated welds were tested and are shown in figure 4.3. The only purpose of measuring the hardness across the weld seam was to display the different material zones.

The experimental fatigue tests were conducted in a load-controlled servo-hydraulic tension testing machine at a loading frequency of  $f = 15 - 30 \text{ s}^{-1}$ . The geometries were tested under three different loading rates, namely: fully reversed loading ( $R = -1$ ), pulsating loading ( $R = 0$ ) and high mean stress (tension-tension,  $R = 0.5$ ) (see table 4.1). The tests were conducted in air, at room temperature ( $20^\circ\text{C}$ ).

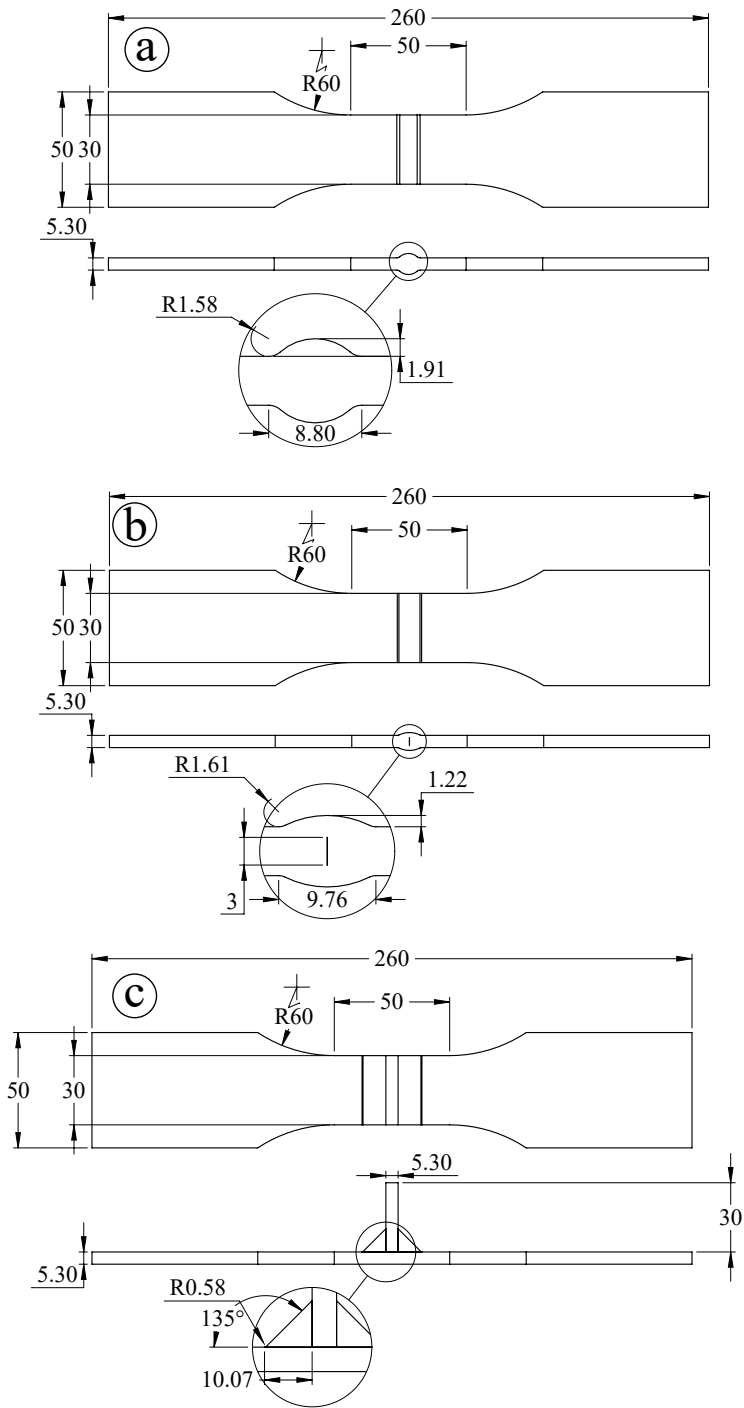


**Figure 4.2:** Mean experimental specimen dimensions. a: Fully penetrated butt welded plate, b: Non-penetrated butt welded plate, c: Plate with welded transverse stiffener

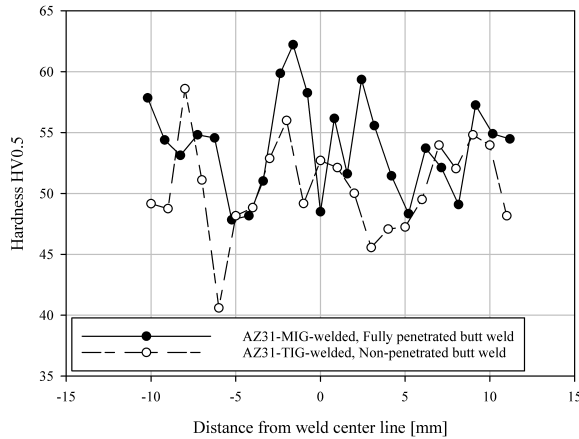


Figure 4.3: Measures weld seam hardness distribution [33]

## 4.2 Numerical Procedure

To fully understand the reaction stresses that a welded joint experiences under cyclic loading, it is essential that the numerical model as accurately as possible portray the physical shape and nature of the specimen used in the experimental investigation. Since most experimental specimens (especially welded specimens) are highly irregular, it is important to have a large number of accurate specimen measurements. These measurements can then be used to find mean values which then specify the dimensions applied in the numerical model. The dimensions used in the numerical analysis are specified in figure 4.2.

To further simplify the numerical model, the following assumptions and simplifications were made: the specimens are portrayed as double symmetric about its centre; the weld seam are portrayed as an even "bump" with a smooth surface and with a constant weld toe opening angle and notch radius; that the loading is under plane strain conditions ( $\varepsilon_{zz} = 0$ ), due to the large in-plane thickness ( $t_z = 30 \text{ mm}$ ). Hence, the model can be simplified to a planar 2D structure; it is assumed that there are no imperfections in the base and weld material; the weld root is portrayed as a crack with no crack tip blunting. The base and weld material, as well as the heat affected-zone, are assumed to have the same/constant material properties (such as Young's modulus and Poisson ratio).

The same numerical model will be used to estimate the resulting ASED under loading for each weld geometry (i.e. three FEM models in total). The loads used are the ones found experimentally and are presented in appendix D. They are applied in the FEA as the stress range,  $\Delta\sigma = 2\Delta\sigma_{a,nom}$  for the R=0 and R=0.5 loading ratios. For R=-1, only the tension part of  $\Delta\sigma$  is considered (i.e.  $\Delta\sigma = \sigma_{a,nom}$ ), because the specimens did not receive post heat treatment to relieve residual stresses from welding. The resulting  $\Delta\bar{W}$  from the applied stress range was then paired with its respective  $N_f$  (number of cycles to failure)

which was found experimentally. This in term will make a scatter plot of  $\Delta\bar{W}$  vs.  $N_f$ . The ASED method is applied to the part of the geometry regarded as most likely to cause the largest stress concentration, and thus the point where a failure is most likely to occur. In the case of the three geometries that were investigated in these numerical analyses, the point of interest were: the weld toe for the fully penetrated butt welded plate and the plate with welded transverse stiffener, which is regarded as notches with a blunt tip; the weld root in the case of the non-penetrated butt welded plate, which is regarded as a sharp crack.

To calculate the resulting  $\Delta\bar{W}$  under loading the *Computer Aided Engineering* (CEA) software Abaqus 6-14 was used.

#### 4.2.1 Finite Element Method Model

As stated earlier, the width of the specimens was far greater than that of their thickness and height, and were therefore presumed to experience plane-strain. Therefore, a three dimensional (3D) to two dimensional (2D) simplification is in order. The specimens were "cut" at the point of constant width of 30 mm so that they would be symmetrical about their center. The total length was then reduced from 260 mm to 50 mm. Further, the center section was reduced to a 2D homogeneous structure with a plane strain width of 30 mm (as per dimensions in figure 4.2). An illustration of this simplification process is shown in figure 4.4. The same method of simplification was applied to all of the geometries.

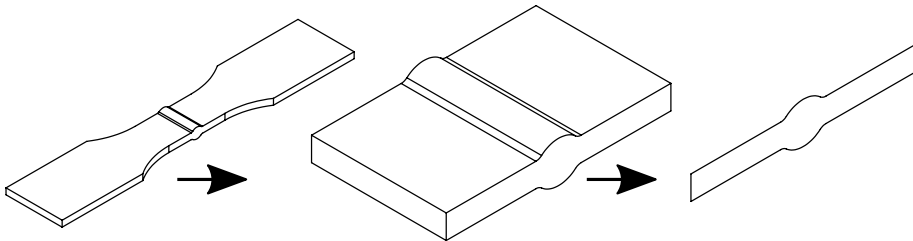


**Figure 4.4:** Model simplification

The material properties applied to the Finite Element Method models (FEM) were in conjunction with those stated in the AZ31 magnesium material properties section, for base metal (table B.1). The material properties used were the AZ31 module of elasticity,  $E = 43 \text{ GPa}$  and Poisson's ratio,  $\nu = 0.35$ . These material properties were used for all FEM models.

Correct meshing is important to obtain realistic and accurate results in a Finite Element Analysis (FEA). Especially in  $\Delta\bar{W}$  analysis, the mesh within the control radius might be important, even though it, in most cases, is presumed to be mesh independent. Therefore, the mesh within the control radius was selected to be quadratic elements set up for plane strain. After determining a  $R_c$ , a mesh sensitivity study was conducted to ensure that the selected element number and size were adequate. The Global mesh size for all three

geometries were 1 mm. The meshes used is shown in figure 4.7, where the control radius is highlighted. The FEM models were partitioned into "SETs", which allows for extraction of the reaction of all elements within the control radius, which defines the boundary of the SET. The  $\Delta\bar{W}$  was extracted from the FEM model employing two parameters from within an in-closed volume limited by the control radius. These two parameters were the Total Elastic Strain Energy (ELSE) which has the unit  $Nmm$ , and Element Volume (EVOL) which has the unit  $mm^3$ . The resulting  $\Delta\bar{W}$  were then calculated using equation 4.1.

$$\Delta\bar{W} = \frac{ELSE}{EVOL} \quad (4.1)$$

### Load and boundary conditions

The boundary conditions and loads selected in the FEA were performed on the premises of best representing the conditions the specimens would experience during the experimental investigation. Since only the central part of the specimens were modelled, it was vital that the "cut" edges acted as they would if the whole specimens were evaluated. To permit this, the two outermost edges (left and right according to fig. 4.5) were applied a *Coupling* constrain. This in terms means that the nodes on the same edge were prevented from moving relative to each other, thus recreating the effect of a un-cut plate. Furthermore, one of the edges was applied a *end-cast* constrain, which prohibits the edge from moving ( $U1 = U2 = 0$ ), thus simulating the constraints caused by the grips of the servo hydraulic testing machine would exercise. The other end of the model was constrained from moving perpendicular to the load direction ( $U2 = 0$ ). Lastly, a negative pressure (tension stress) was applied in  $U1$  direction. The load and boundary conditions are illustrated by figure 4.5. Since the FEM models are 2D structures, there was no need to constrain the model in the out-of-plane direction ( $U3$ ). The same boundary conditions and load setup was applied for all of the FEM models. In the case of the non-penetrated butt welded plate, the weld root of the joint (in the center) was modeled as a sharp crack/seam with a length of 3 mm (as per fig. 4.2 b) as illustrated by figure 4.9.

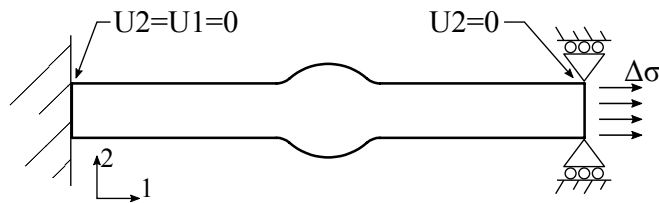


**Figure 4.5:** Boundary conditions and load application to FEM models.  $U1$  and  $U2$  is displacement in 1 and 2 direction

### Control Radius, $R_c$

The control radius is as mentioned earlier in section 2.3.3, the parameter in which specifies the in-closed volume that is used when obtaining the ASED.  $R_c$  can be regarded as one of the most critical parameters in the use of ASED, and therefore the correct choice of  $R_c$

is vital in getting accurate  $\Delta\bar{W}$  results. It is essential that the selected  $R_c$  not to be too large compared to the evaluated geometry. Since the premise of  $\Delta\bar{W}$  is to only consider the effect of local strain energy surrounding a notch or crack. If too large a  $R_c$  is selected the system can no longer be regraded as local, but rather a global one.

Traditionally, calculations of  $R_c$  for structures under fatigue loading have been obtained with equation 2.20. This equation is based on the resulting NSIF in a V-notched specimen, loaded at the stress range for the fatigue limit ( $N_A = 5 \cdot 10^6$  cycles) of a welded specimen where the welds are ground smooth (i.e. a un-notched specimen) [3]. As in this case, the stress range at the fatigue limit for AZ31 magnesium alloy with a ground flush weld is unknown, making this approach to determine  $R_c$  impossible.

The intention of ASED in fatigue life assessment is to develop a common criterion which is independent of geometry, loading mode, and loading ratio. The selected  $R_c$  should then be of an order that when applied to different geometries, the resulting  $\Delta\bar{W}$  vs.  $N_f$  should follow the same path. It should also then result in a  $\Delta\bar{W}$  vs.  $N_f$  plot with a minimum of data scattering when a regressional fit is conducted across both geometries and loading ratios. Therefore, the proposed way of finding an appropriate  $R_c$  is to do multiple numerical analyses of the experimental fatigue data with a incrementally changing  $R_c$  until the a value which yields the best fit for all geometries is found.

The first step in this process is to locate the correct placement of the control radius centre. In the case of the non-penetrated butt welded plate, this is quit strength forward as the critical part of the geometry is the weld root, which is portrayed as a sharp crack. The centre of  $R_c$  is therefore located at the crack tip. In the case of the two geometries with a blunt notch,  $R_c$  is located with its centre on the notch bisector line ( $\gamma$ ) and at a distance  $r_0$  from the notch tip.  $r_0$  is a parameter based on the notch opening angle ( $2\alpha$ ) and the notch tip radius ( $\rho$ ) and calculated from equation 2.12. In the case of a notch with a blunt tip,  $R_c$  is the distance between the notch tip and the radius, along the notch bisector line (as illustrated by figure 2.9).

As  $r_0$  is based on  $2\alpha$ , it has to be determined for the two geometries where the weld toe is considered as the most critical<sup>2</sup>. The problem with determining this angle for a butt weld is that the weld seam has an arc shape and thus  $2\alpha$  would increase as from where the reference point lies. Suggested best practice for determining  $2\alpha$  in such a case is to start a line from the intersection point of the weld seam arc and the plate top surface. Then the line is set so that it is tangent to the weld seam arc, as illustrated by figure 4.6. In the case of the fully penetrated butt welded plate, this results in an opening angle of  $2\alpha = 131.7^\circ$  and a notch bisector line angle of  $\gamma = 114.15^\circ$  respectively. In the case of the plate with welded transverse stiffener, where to plates that are placed normal to each other is welded together with a fillet weld, the opening angle has traditionally been portrayed as  $2\alpha = 135^\circ$  and notch bisector line angel at  $\gamma = 112.5^\circ$  [30].

---

<sup>2</sup>i.e. fully penetrated butt welded plate and plate with welded transverse stiffener

The placement of  $R_c$  for the three geometries are illustrated by figure 4.7 to 4.10, the calculated values for  $r_0$  are presented in table 4.5

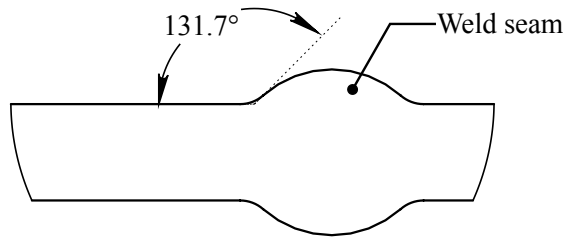


**Figure 4.6:** Notch opening angle ( $2\alpha$ ) for fully penetrated butt welded plate

**Table 4.5:** Blunt notch compensation parameters

Geometry	Notch tip radius, $\rho$	Notch opening angle, $2\alpha$	$r_0$
Fully penetrated butt welded plate	1.58 mm	131.7°	0.33 mm
Plate with welded transverse stiffener	0.58 mm	135.0°	0.12 mm

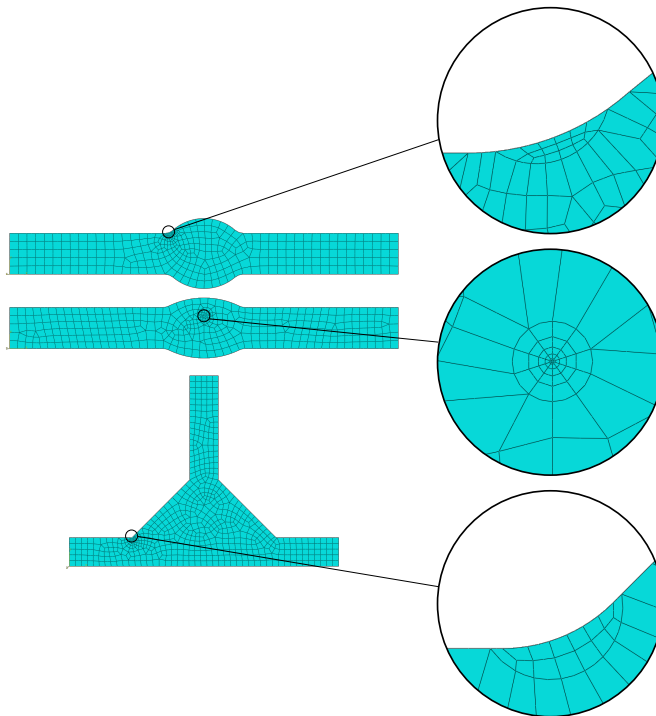


**Figure 4.7:** Meshed geometries. From top: fully penetrated butt welded plate, non-penetrated butt welded plate and plate with welded traversal stiffener where the control radius,  $R_c$  is highlighted

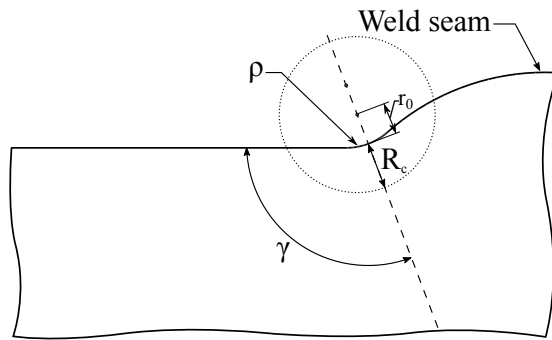


**Figure 4.8:** Placement of control radius for fully penetrated butt welded plate with dimensions:  $R_c = 0.15 \text{ mm}$ ,  $\rho = 1.58 \text{ mm}$ ,  $r_0 = 0.33 \text{ mm}$  and  $\gamma = 114.15^\circ$

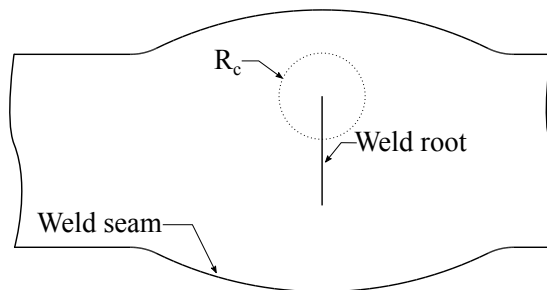


**Figure 4.9:** Placement of control radius for non-penetrated butt welded plate with dimension:  $R_c = 0.15 \text{ mm}$

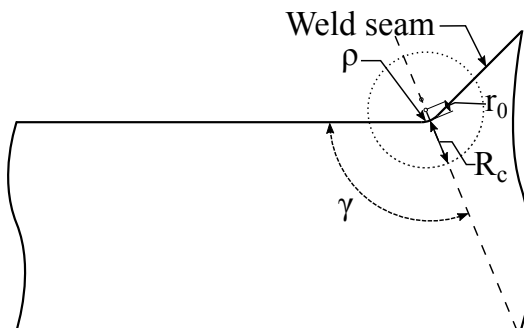


**Figure 4.10:** Placement of control radius for plate with welded transversal stiffener with dimensions:  $R_c = 0.15 \text{ mm}$ ,  $\rho = 0.58 \text{ mm}$ ,  $r_0 = 0.12 \text{ mm}$  and  $\gamma = 112.5^\circ$

As a reference point for the incremental approach to identifying an appropriate  $R_c$  for welded AZ 31 magnesium alloy,  $R_{cs}$  used for materials with similar elastic material properties were consulted. Materials with similar material properties where ASED have been extensively used on welded joints are aluminum and aluminum alloys [4, 5]. Aluminum and aluminum alloys generally have the elastic properties of: Young's modulus  $E \approx 69 \text{ GPa}$  and Poisson ratio  $\nu \approx 0.3$ , compared to  $E \approx 43 \text{ GPa}$  and  $\nu \approx 0.35$  for AZ31 magnesium alloy. [40]. The suggested control radius for welded aluminum joints found in the literature is  $R_{c,Al} = 0.12 \text{ mm}$  [4].

In figure 4.11 excerpt from the incremental approach to establish  $R_c$  is presented. As a measurement of the quality of  $R_c$ , the coefficient of determination,  $R^2$  is used. This investigation indicates that as the control radius decreases the coefficient of determination increases. Too small of an  $R_c$  would be impractical. A compromise of  $R_c = 0.15 \text{ mm}$  was therefore chosen as an adequate value for the control radius. It yielded a coefficient of determination of  $R^2 = 0.152$ .

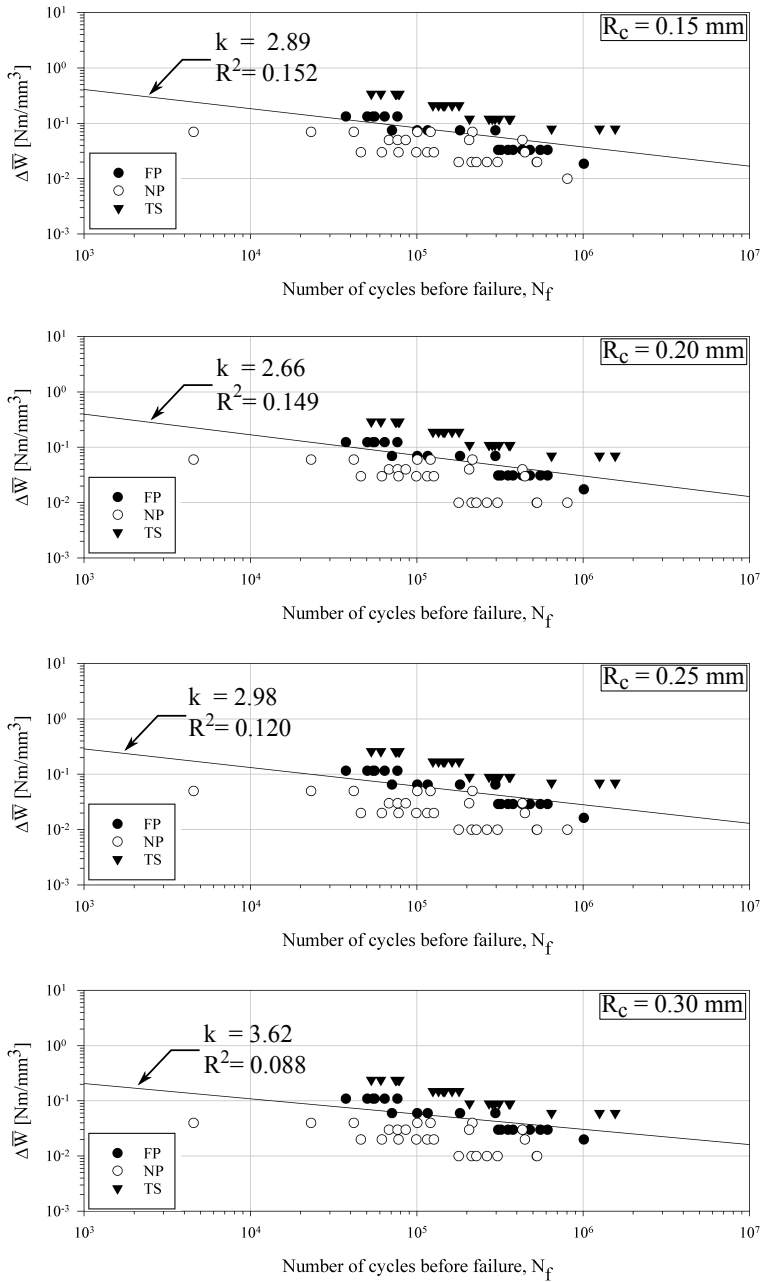


**Figure 4.11:** Resulting data scatter with incrementally changing  $R_c$ , for welded specimens under  $R = 0$  loading. FP: Fully penetrated butt welded plate; NP: Non-penetrated butt welded plate; TS: Plate with welded transverse stiffener

### Mesh validation

As stated earlier, ASED is generally regarded as mesh-independent to a certain degree. Nevertheless, a mesh sensitivity study was conducted as to verify that the number of elements present within the control radius ( $R_c = 0.15 \text{ mm}$ ) were sufficient. Such a study is done by gradually increasing the number of elements present within the control radius and then recording the resulting  $\Delta\bar{W}$  within. The result of this investigation for the plate with welded transverse stiffener is shown in figure 4.12. The study indicated that by reducing the number of elements from 14 to 6, it resulted in a change of extracted  $\Delta\bar{W}$  by  $\sim 0.47\%$  and by increasing the number of elements from 6 and up, the change was  $0.025\%$ . Such a small change in  $\Delta\bar{W}$  indicated that the number of elements present within the control radius was to some degree insignificant. The number of elements that were used in the FEM models for the numerical investigation are shown in table 4.6. The selection was done on the grounds of having a sufficient amount of elements as to capture the contour of the notch/crack without the CEA software (Abaqus) giving warnings about "bad elements". Abaqus defines "bad elements" as elements that do not fit the following criterion: smaller face corner angle, elements containing faces where two edges meet at an angle smaller than a specified angle; larger face corner angle, elements containing faces where two edges meet at an angle larger than a specified angle; aspect ratio, elements with an aspect ratio larger than a specified value. The aspect ratio is the ratio between the longest and shortest edge of an element; short edge, elements with an edge shorter than a specified value; shape factor, elements with a normalized shape factor smaller than a specified value[41].

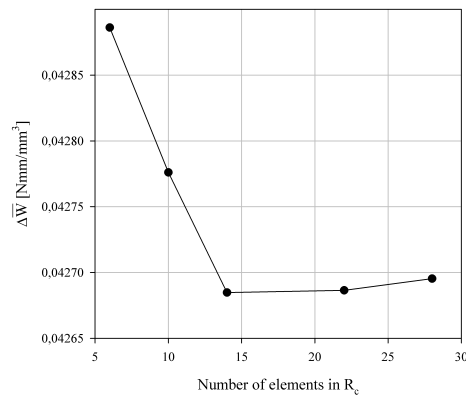


**Figure 4.12:** Effect of the number of elements in the control radius,  $R_c$

**Table 4.6:** Number of elements within control radius of FEM models

Geometry	Number of elements within control radius, $R_c$
Fully penetrated butt welded plate	16
Non-penetrated butt welded plate	40
Plate with welded transverse stiffener	14

### 4.3 Analytical Evaluation

An analytical evaluation of implementing ASED as a fatigue criterion for welded AZ31 magnesium alloy joints, might give an insight to the correlation between the results found numerically and the formulation presented in the literature. The analytical evaluation used is based on the SIF and the notch tip max stress ( $\sigma_{max}$ ).

#### 4.3.1 An analytical approach to ASED

The analytical approach to determine ASED is applied to one of the geometries considered in the numerical investigation, namely the non-penetrated butt welded plate. Since its critical feature is the weld root. The weld root, in this case, can be perceived as a sharp crack under pure mode I loading (crack opening), which facilitates an easy and accurate obtaining of SIF.

Calculating  $\Delta\bar{W}$  from SIF for welded joints subjected to cyclic loading was done through a variation of the formulation for  $\bar{W}$  (eq. 2.17), where stress range was used instead of static stress. The formulation for  $\Delta\bar{W}$  is given by equation 4.2, where:  $c_w$  is a coefficient which accounts for the influence of nominal stresses on R, for a welded joint that is subjected to post-welding heat-treatment. In the case of "as welded" joints (no post welding heat-treatment) this coefficient is  $c_w = 1$ ;  $e_1$  and  $e_2$  are functions that are dependent of notch opening angle, for cracks under mode I loading (as in the case of the non-penetrated butt welded plate) only  $e_1$  is considered and was equal to 0.133;  $\Delta K_1$  and  $\Delta K_2$  are SIF;  $\lambda_1$  and  $\lambda_2$  are functions of the notch opening angel, and for cracks they are equal to 0.5 (see fig. 2.8); The same control radius that was found in the numerical investigation was applied in the analytical investigating ( $R_c = 0.15 \text{ mm}$ ) [5].

$$\Delta\bar{W}_K = c_w \left\{ \frac{e_1}{E} \left[ \frac{\Delta K_1}{R_c^{1-\lambda_1}} \right]^2 + \frac{e_2}{E} \left[ \frac{\Delta K_2}{R_c^{1-\lambda_2}} \right]^2 \right\} \quad (4.2)$$

In the case of the non-penetrated butt welded plate, the SIF ( $\Delta K_1$ ) was determined by FEA. The same model and boundary conditions as in the numerical investigation were used, only with other meshing parameters at the weld root (i.e., the crack tip). The crack tip of the non-penetrated butt welded plate experiences pure mode I (crack opening,  $\Delta K_2 = 0$ ) and thus only  $\Delta K_1$  needed to be determined. FEA were conducted at a unit stress range of  $\Delta\sigma_{unit} = 1 \text{ MPa}$  tension, and then converted over to  $\Delta\bar{W}_{unit}$  form via equation 4.2.

The unit  $\Delta\bar{W}_{K,unit}$  was then applied to the same stress ranges used in the numerical investigation, and then paired with its respective  $N_f$ . This was done by an interpretation of the equation for  $\bar{W}_c$  (2.19). A relation between two  $\Delta\bar{W}$  and their equivalent stress range ( $\Delta\sigma$ ) may be found as the Young's modulus is constant, the relationship of  $^{1/2}E$  is also constant, thus equation 4.3 was used.

$$\Delta\bar{W} = \frac{1}{\left(\frac{\Delta\sigma_{unit}}{\Delta\sigma}\right)^2} \cdot \Delta\bar{W}_{K,unit} \quad (4.3)$$

### Determining of Stress Intensity Factors

An important part of the analytical evaluation of  $\Delta\bar{W}$  is the SIF. To obtain a correct value for  $\Delta\bar{W}_{K,unit}$ , the collected SIF from the FEA had to be an accurate representation of the stresses at the weld root. As the sharp tip of the weld root caused a stress singularity, the resulting stresses obtained through FEM is highly mesh dependent. For this reason, it is important that sufficient meshing parameter was chosen so that the obtained SIF would be accurate. This was done through a mesh sensitivity study. The number and size of the elements surrounding the weld root tip were gradually increased, and the resulting SIF recorded (see figure 4.14). The SIF was obtained through CEA software Abaqus, which uses a contour integral to determine the resultant SIF. A sweep mesh with 2D quadratic elements set for plain strain was selected to encircle the weld root tip by a radius of 1 mm. The model was subjected to a unit load of 1 MPa tension.

The results from the mesh sensitivity study is shown in figure 4.13. As can be seen from the figure, when the number of elements went from 1125 to 1500 a drop in the extracted SIF was experienced. The study showed that 1500 elements were sufficient, as the change in SIF by increasing the number of elements was only 0.053%. The resulting SIF used to calculate  $\Delta\bar{W}_{K,unit}$  hence was  $\Delta K_{1,unit} = 1.860 \text{ MPa}\sqrt{\text{mm}}$ .

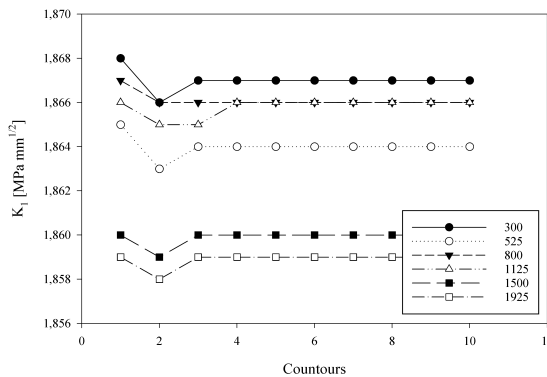


**Figure 4.13:** Mesh sensitivity of Stress intensity factor the weld root of the non-penetrated welded plate under a unit load of 1 MPa. The legends show the applied number of elements

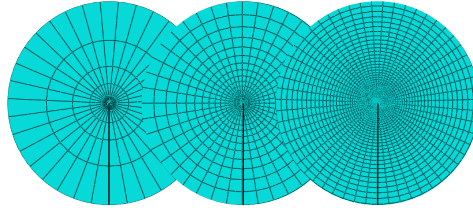


Figure 4.14: Coarse to fine mesh, weld root

### 4.3.2 An analytical approach to determine maximum blunt notch stress from $\overline{W}$

A comparison between the maximum blunt notch stress found via a fine mesh FEA and one that was found analytically, could give valuable insight into the validity of the parameters used in the numerical investigation, for example, the critical radius,  $R_c$ . This comparison was done to the fully penetrated butt welded plate, as it had the largest blunt notch (i.e., the weld toe) radius ( $\rho = 1.58 \text{ mm}$ ), and hence it was the most applicable for such an assessment. The same FEM model, boundary conditions, and control radius as in the numerical investigation was used. The assessment was conducted under a unit load of  $\sigma_{unit} = 1 \text{ MPa}$  tension, which in terms gave an extracted value of  $\overline{W}_{unit} = 2.09 \cdot 10^{-5} \text{ Nmm} / \text{mm}^3$ .

Determining the maximal notch stress through the use of  $\overline{W}$  can be done with the formulation presented in equation 4.4. Where  $E_1^{(e)}$  is a parameter which is based on the Young's modulus, max notch stress, notch radius, and the notch opening angel.  $\Omega$ , on the other hand, is the area defined by the control radius  $R_c$ . This expression has been generalized to the parameters  $F(2\alpha)$  which is dependent of the notch opening angle and  $H(2\alpha, R_c/\rho)$  which depends on the notch opening angle and the relationship between the control radius and the blunt notch radius. For this assessment, these values were determined by linear interpolation and extrapolation of the values presented in Appendix A, which gave an  $F(2\alpha) \approx 1.268$  and  $H(2\alpha, R_c/\rho) \approx 0.325$ , respectively. [42]

$$\overline{W}_1^{(e)} = \frac{E_1^{(e)}}{\Omega} = F(2\alpha) \cdot H(2\alpha, R_c/\rho) \frac{\sigma_{max}^2}{E} \quad (4.4)$$

The maximum stress that was determined is the one that acts orthogonally to the blunt notch bisector line. In the case of the weld toe (which is perceived as a blunt notch) the maximum orthogonal stress was found by determining a polar coordinate system with its centre at the middle of the blunt notch tip, and with the R-axis parallel to the notch bisector line (as illustrated by fig. 4.15).

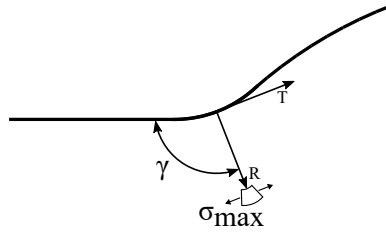


**Figure 4.15:** Maximum orthogonal stress relative to centre of notch and the notch bisector line  $\gamma$

#### Determining of $\sigma_{max}$ from FEA

Stresses in an FEA can be highly mesh-dependent. Therefore, it is important that the right meshing parameters be selected. This is so that a viable stress result may be extracted from the analysis. It was therefore conducted a mesh sensitivity study of the area surrounding the blunt notch tip. A gradually finer mesh was applied and the resulting stress recorded (see figure 4.16). The mesh used was a swept mesh with 2D quadratic elements set up for plain strain.  $\sigma_{max}$  was determined by placing the FEA reference point at the centre for the blunt notch with a polar coordinate system, where R-axis was collinear to the notch bisector line. The resulting maximum stress was then  $\sigma_{max} = \sigma_{22,max}$ . The sensitivity study was conducted with the number of elements ranging from 20 to 3000, in an area with a radius of 1.5 mm from the blunt notch tip. Results from this study is shown in figure 4.17. It shows that when the number of elements exceeds  $\sim 1600$ , the resulting  $\sigma_{22,max}$  is stable at 1.606 MPa.

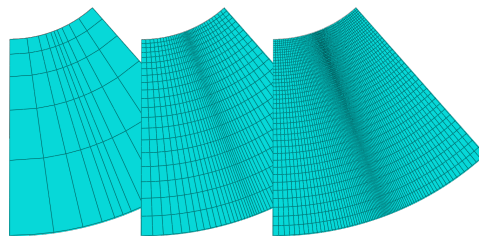


**Figure 4.16:** Coarse to fine mesh, weld toe

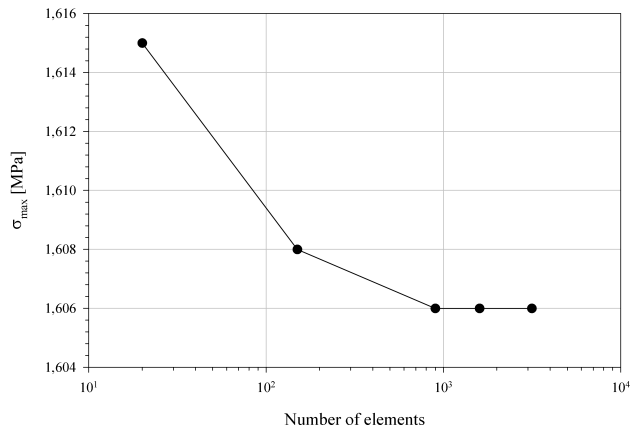


**Figure 4.17:** Number of elements vs. resulting orthogonal max stress

# Chapter 5

## Results

### 5.1 Experimental Results

Experimental results from cyclic loading of welded joints made of AZ31 magnesium alloy are presented in figure 5.2 to 5.4. The results are presented in the form of S-N curves in a double logarithmic scale. The results is divided into three separate plots, one for each loading ratio. The results for each geometry has a power law regression line fitted, where run-out specimens ( $N > 5 \cdot 10^6$  cycles) has been excluded. Figure 5.1 shows the most common failure modes for each geometry. Detailed results are available in Appendix C.



**Figure 5.1:** Failure points of the welded experimental specimens. (a) full penetration butt welded plate (crack initiation at weld toe), (b) non-penetrated butt welded plate (crack initiation at weld root), (c) transverse stiffener (crack initiation at weld toe). Image courtesy of Özler Karakaş [35]

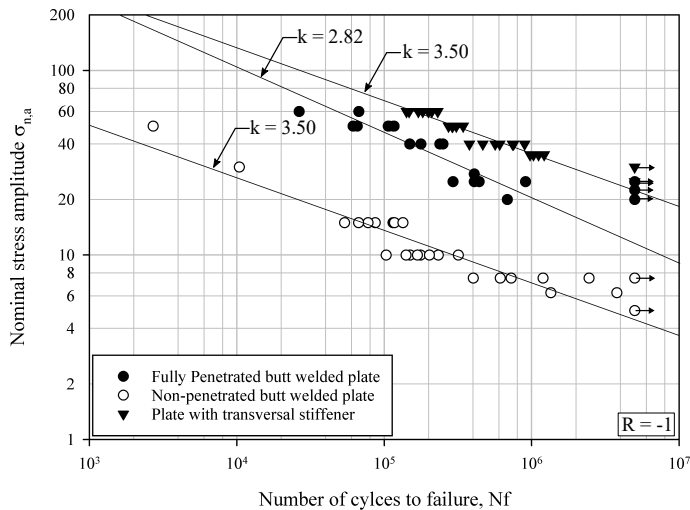


**Figure 5.2:** S-N curves for welded joints of AZ31 magnesium alloy under fully reversed loading,  $R=-1$

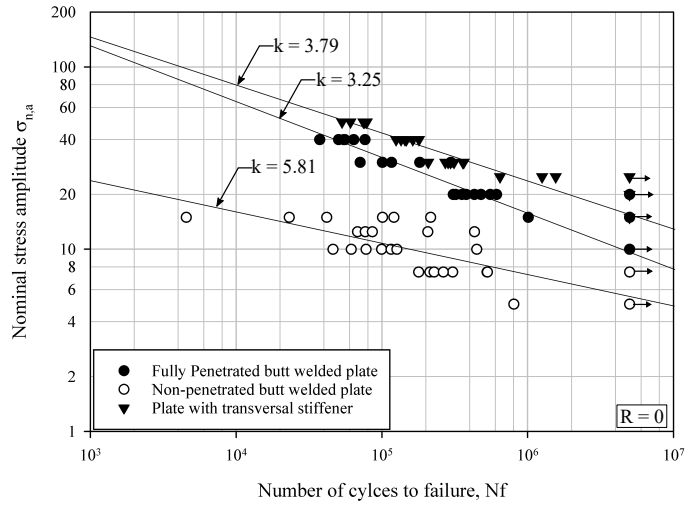


**Figure 5.3:** S-N curves for welded joints of AZ31 magnesium alloy under pulsating loading,  $R=0$

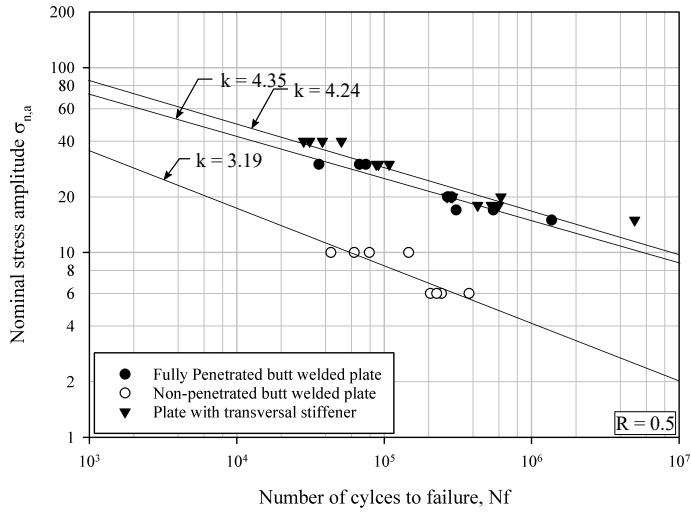


**Figure 5.4:** S-N curves for welded joints of AZ31 magnesium alloy under high mean stress,  $R=0.5$

## 5.2 Numerical Results

Results from the numerical investigation of ASED as a fatigue criterion for welded joints made of AZ31 magnesium alloy are shown in figure 5.5 to 5.11. The results are presented in the form of  $\Delta\bar{W} - N_f$  plots with a double logarithmic scale. Results are divided into six plots, one for each loading ratio, one for each geometry (regardless of loading ratio) and one that is a plot of all resultant  $\Delta\bar{W}$  regardless of loading ratio. The plots have been fitted with a power law regression line where run-out specimens have been excluded ( $N > 5 \cdot 10^6$  cycles). The slope and coefficient of determination  $R^2$  for the power law regression lines are highlighted in the plots, as well as the applied  $R_c$ . Detailed results are available in Appendix C.

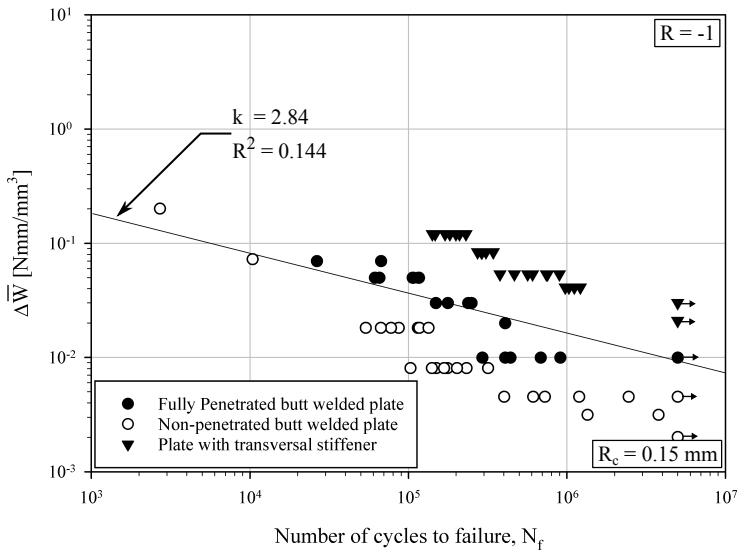


**Figure 5.5:**  $\Delta\bar{W} - N$  curves for welded joints of AZ31 magnesium alloy under fully reversed loading,  $R=-1$ .  $\Delta\bar{W}_{R=-1} = (2.123) \cdot N_f^{-0.352}$

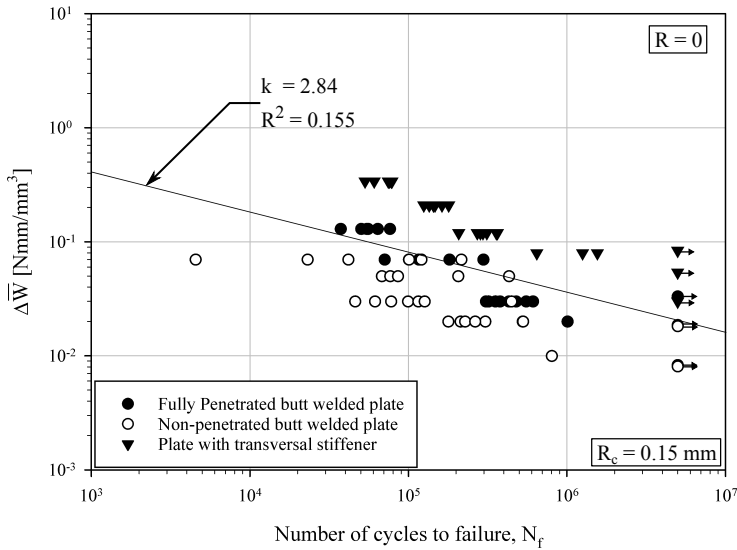


**Figure 5.6:**  $\Delta\bar{W}$  - N curves for welded joints of AZ31 magnesium alloy under pulsating loading,  $R=0$ .  $\Delta\bar{W}_{R=0} = (4.736) \cdot N_f^{-0.352}$

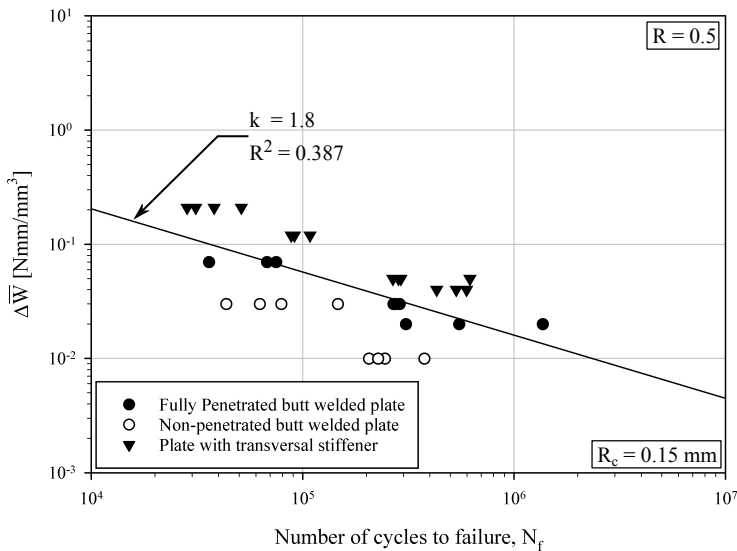


**Figure 5.7:**  $\Delta\bar{W}$  - N curves for welded joints of AZ31 magnesium alloy under high mean stress,  $R=0.5$ .  $\Delta\bar{W}_{R=0.5} = (33.261) \cdot N_f^{-0.553}$

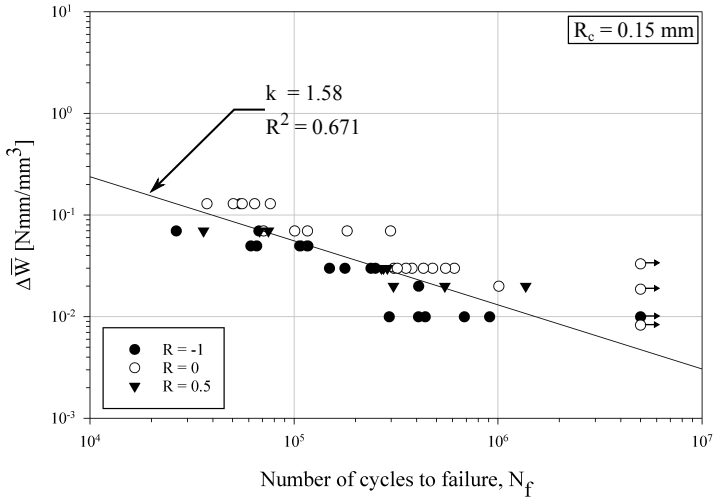


**Figure 5.8:**  $\Delta\bar{W}$  -  $N$  curve for fully penetrated butt welded plate regardless of mean stress.  $\Delta\bar{W} = (80.7) \cdot N_f^{-0.631}$

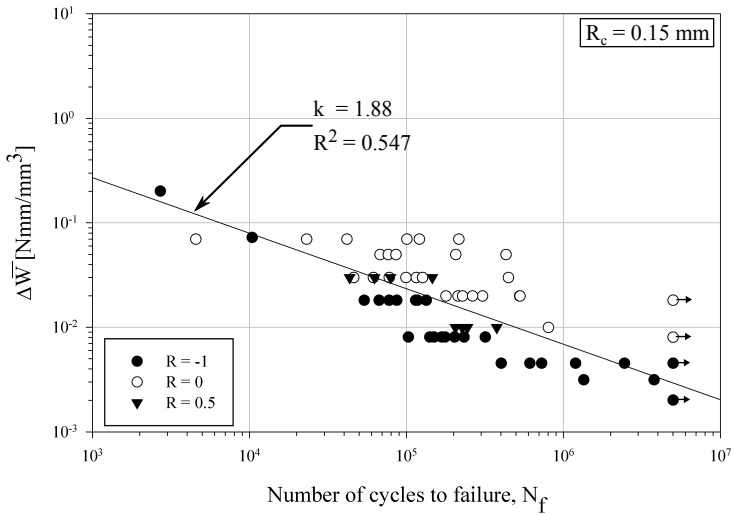


**Figure 5.9:**  $\Delta\bar{W}$  -  $N$  curve for non-penetrated butt welded plate regardless of mean stress.  $\Delta\bar{W} = (10.9) \cdot N_f^{-0.531}$

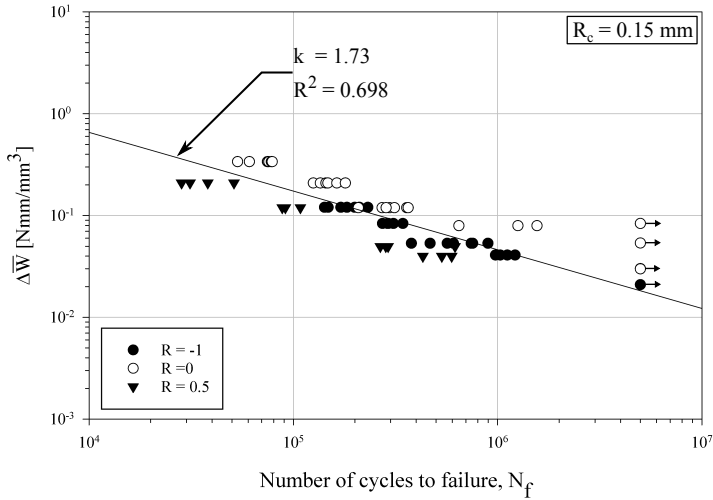


**Figure 5.10:**  $\Delta\bar{W}$  -  $N$  curve for plate with welded transverse stiffener regardless of mean stress.  
 $\Delta\bar{W} = (134.6) \cdot N_f^{-0.577}$

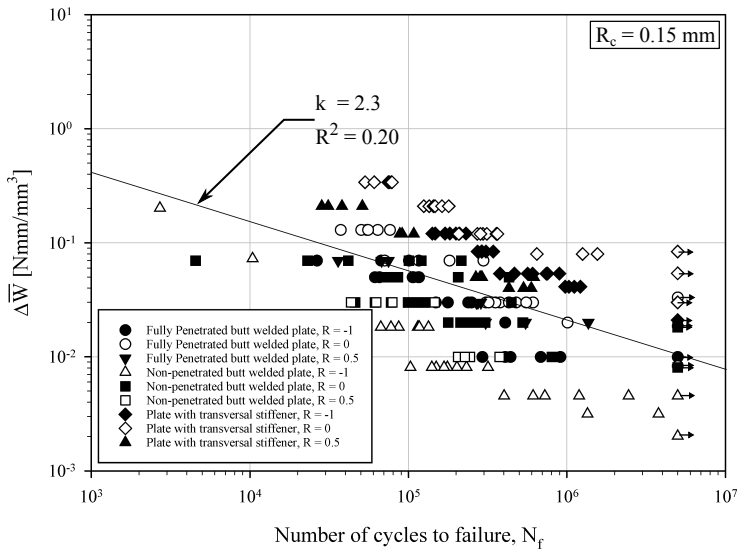


**Figure 5.11:**  $\Delta\bar{W}$  -  $N$  curve for welded joints of AZ31 magnesium alloy regardless of mean stress.  
 $\Delta\bar{W} = (8.584) \cdot N_f^{-0.435}$

### 5.3 Analytical Results

Results from the analytical evaluation of  $\Delta\bar{W}$  and  $\bar{W}$  are presented in figure 5.12 and table 5.1. Figure 5.12 is a plot in double logarithmic scale of all test results for the non-penetrated butt welded plate, where  $\Delta\bar{W}$  was calculated from SIF extracted via FEA. The results have been fitted with a power law regression line, where the slope and coefficient of determination  $R^2$  are highlighted.

Table 5.1 shows the results from the analytical calculation of the blunt notch max stress for the weld toe of the fully penetrated butt welded plate.  $\sigma_{\bar{W},max}$  is the stress found through the analytical approach based on the obtained  $\bar{W}$  for a unit load of  $\sigma_{unit} = 1 \text{ MPa}$  and  $\sigma_{max}$  is the maximum blunt notch stress found through FEA with a traditional fine mesh approach under a unit load of  $\sigma_{unit} = 1 \text{ MPa}$ . The discrepancy between the two is also listed in the table 5.1. Detailed results are available in Appendix D.

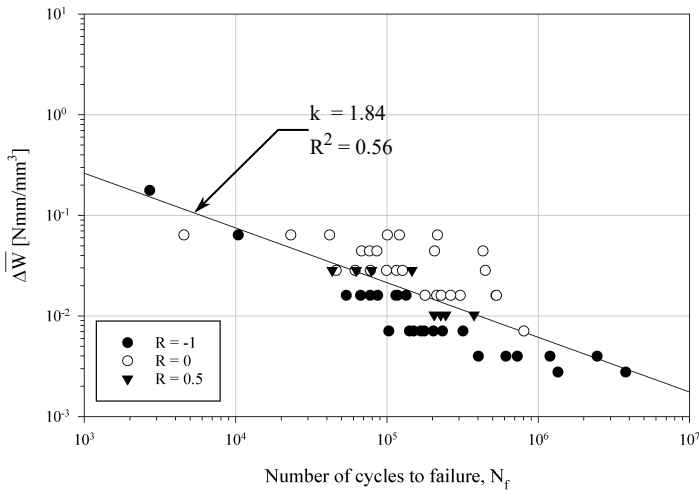


**Figure 5.12:** Analytically derived  $\Delta\bar{W}$  - N curve for non-penetrated butt welded plate

**Table 5.1:** Numerically and analytically derived weld toe max stress for the fully penetrated butt welded plate

$\sigma_{\bar{W},max}$ [MPa]	$\sigma_{max}$ [MPa]	Discrepancy
1.477	1.606	8.06%



# Chapter 6

## Discussion

### Evaluation of experimental results

The experimental result gathered from subjecting welded joints of AZ31 magnesium alloy to cyclical loading indicates that this alloy as with other, experience drastically different fatigue life expectancy dependent of the joining geometry and loading ratio. As can be seen from figure 5.2 to 5.4, none of the power law regression curves were applicable for another geometry or even the same geometry, but at another loading ratio. This might be because of critical weld geometries such as weld toe radius, weld toe opening angle and weld root tip. These parameters generate different amounts of stress concentrations depending of their size and geometry and, hence, a different lifetime expectancy.

The data scatter was relatively small for all geometries, which indicates that the specimens used had quite a uniform geometry with few defects in the weld. The only exceptions were the non-penetrated butt welded plate and fully penetrated butt welded plate under fully reversed loading ( $R=-1$ ). These specimens tended to fail earlier than  $N_f < 10^4$ . This scatter might be due to distortion or eccentricity as a result of welding. In the compression regime of  $R=-1$  this distortion or eccentricity causes the specimens to slightly bend.

Figure 5.1 shows the most common failure modes for each geometry, which indicates that: for the fully penetrated butt welded joint the critical feature is the notch caused by the weld seam; for the non-penetrated butt welded plate the critical feature is the weld root caused by the lack of penetration; for the plate with the welded transverse stiffener the critical feature is the weld toe caused by the fillet weld.

As the failure always occurred in or near the weld (the areas that have been melted during welding or were in the HAZ), it indicates that rolling direction (grain structure caused by rolling) of the AZ31 magnesium alloy sheet had little influence on the fatigue life expectancy, as this area has been victim of re-crystallization after welding, so that the original grain structure from rolling is removed.

The fatigue strength at  $N_f = 2 \cdot 10^6$  for each geometry and loading rate is evaluated and are presented in table 6.1.

**Table 6.1:** Fatigue strength at  $N_f = 2 \cdot 10^6$

Geometry		Butt weld, fully penetrated	Butt weld, non-penetrated	Transverse stiffener
$R = -1$	$\Delta\sigma_{n,2 \cdot 10^6} = 32.1 \text{ MPa}$	$\Delta\sigma_{n,2 \cdot 10^6} = 11.6 \text{ MPa}$	$\Delta\sigma_{n,2 \cdot 10^6} = 58.5 \text{ MPa}$	
$R = 0$	$\Delta\sigma_{n,2 \cdot 10^6} = 25.6 \text{ MPa}$	$\Delta\sigma_{n,2 \cdot 10^6} = 12.9 \text{ MPa}$	$\Delta\sigma_{n,2 \cdot 10^6} = 39.6 \text{ MPa}$	
$R = 0.5$	$\Delta\sigma_{n,2 \cdot 10^6} = 25.6 \text{ MPa}$	$\Delta\sigma_{n,2 \cdot 10^6} = 6.70 \text{ MPa}$	$\Delta\sigma_{n,2 \cdot 10^6} = 28.7 \text{ MPa}$	

### Evaluation of numerical results

The numerical investigation of the fatigue strength of welded joints made from AZ31 magnesium alloy with ASED as a fatigue criterion shows a clear trend. A comparison of the power law regression line for  $R=-1$  and  $R=0$  (figure 5.5 and 5.6) show that both has the same slope of  $k = 2.84$ .  $R=0.5$ , on the other hand, has a slope of  $k = 1.8$ . It is difficult to distinguish which parameter that might have caused this discrepancy amongst the two. One factor might be that the number of specimens considered for both  $R=0$  and  $R=-1$  is substantial compared to that of  $R=0.5$ , which again can result in a less accurate result.

In figure 5.8 to 5.10 the resulting  $\Delta\bar{W} - N_f$  relationship for each respective geometry is plotted, regardless of loading ratio. The resultant power law regression line for the three have a slope and fit in the range of  $k \approx 1.58 - 1.88$ , and  $R^2 \approx 0.547 - 0.698$ , respectively. A rough estimate of the data scatter ( $T_{\Delta\bar{W}}$ ) puts it 6.6 for the fully penetrated butt weld, 12.0 for the non-penetrated butt weld and 4.6 for the transversely stiffener.

The slope of the global power law regression line for AZ31 is at  $k = 2.3$ , and its fatigue strength at  $N_f = 2 \cdot 10^6$  is  $\Delta\bar{W} = 15.59 \cdot 10^{-3} \text{ Nmm} / \text{mm}^3$ . When the the slope of the global plot is compared to the slope for welded joints made of aluminum alloys, it is apparent that they are nearly the same. Welded joints made from aluminum alloys have been found to have a slope of  $k \approx 2.24$ <sup>1</sup>. A comparison between the global  $\Delta\bar{W} - N_f$  plot and the mean regression line with probability lines (2.3% -97.7% probability) for welded joints of aluminum alloy are shown in figure 6.1. As can be seen, the  $\Delta\bar{W}$  for AZ31 are generally lower then that of aluminum alloys, which might be due to that aluminum has a higher Young's modulus ( $\sim 69 \text{ GPa}$ ) and uses a smaller control radius ( $0.12 \text{ mm}$ ) than that of AZ31 ( $43 \text{ GPa}$  and  $R_c = 0.15 \text{ mm}$ ).

Also, apparent by the comparison done in figure 6.1 is that the scatter in  $\Delta\bar{W}$  is quite large for AZ31. A rough estimate puts  $T_{\Delta\bar{W}}$  at approximately  $\sim 30$  (5%-95% probability) versus 3.2 (2.3%-97.3% probability) for aluminum. This relatively large scatter was consistent for all of the AZ31  $\Delta\bar{W} - N_f$  result plots (fig 5.5 - 5.11, except for the geometry specific plots). The main culprit for this large scatter is that the  $\Delta\bar{W}$  results for plates with a welded transverse stiffener has a significantly higher value of  $\Delta\bar{W}$  compared to those for the two other geometries.

---

<sup>1</sup>Referring to the paper by P. Livieri *at.al* which was reviewed earlier in the thesis

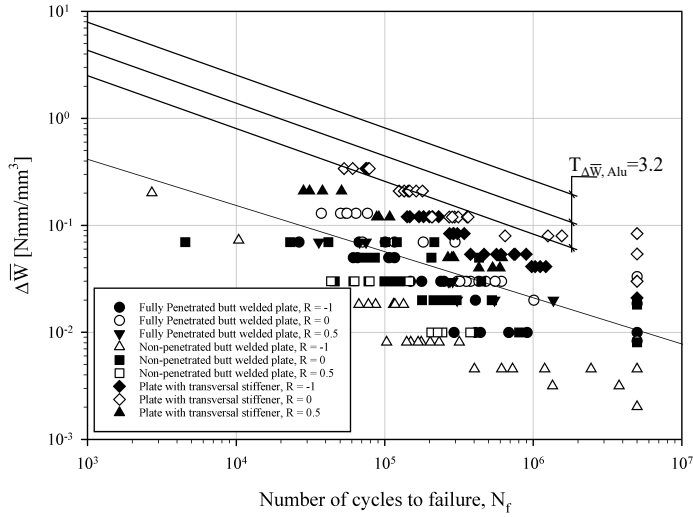


**Figure 6.1:** Comparison of  $\Delta\bar{W} - N_f$  for AZ31 magnesium alloy and regression line for welded aluminum joints [4]

It might be multiple factors that govern this trend of a higher  $\Delta\bar{W}$  value for the transverse stiffener specimens. Some factors that might have influenced this is:

- Distortion caused by welding: the plate with a welded transverse stiffener consists of two parts, one whole load-carrying plate and a smaller plate that is welded on perpendicular to the main plate with two fully penetrating fillet welds. For the two butt welded plates, this load-carrying section of the joint consists of two separate pieces welded together. This production method will in terms create a larger amount of distortion or eccentricity in the specimens during welding relative to the amount that occurs in the plate with the transverse stiffener. This phenomenon is due to that when welding a butt weld, it is nearly impossible to align the two halves perfectly. The effect of this distortion is made apparent in loading ratios where the load is near or in the compression regime, as in  $R=-1$  and  $R=0$ . Compression loading might cause a slight bending moment to occur, and any misalignment will amplify this effect. Misalignment can thus reduce the fatigue life of such specimens. As can be seen from figure 5.5 to 5.7, when the mean stress increases the amount of scattering between the three geometries decreases.
- Inaccurate and/or misinterpretation of the experimental specimen measurements: the geometry of the weld greatly affects the amount of resultant stress concentration and stress intensity that occurs when a specimen is loaded. Important parameters being the notch opening angel (weld toe opening angle) and the blunt notch tip radius (weld toe radius). If one or both of these parameters are incorrectly interpreted or inaccurately measured, it will result in that the model used in the FEA has a smaller/larger notch opening angle ( $2\alpha$ ) or a smaller/large blunt notch radius ( $\rho$ ),

which will in-turn affect the resultant  $\Delta\bar{W}$ . This is one of the disadvantages of interpreting experimental fatigue data that is acquired externally, presented with geometric measurements. Application of ASED as a fatigue criterion in the literature is generally based on fatigue data presented in NSIF versus the number of cycles to failure form. A parameter which gives little room for misinterpretation, and is probably a better approach when evaluating experimental data acquired externally.

A comparison of the slope found for the mean stress-specific plots, the global plot, and the geometry specifics plots, shows that there is a discrepancy amongst them. This discrepancy might indicate that, because of the relatively large scatter in the mean stress-specific plots and the global plot, the resultant power law regression have overestimated its slope, and that the correct slope of  $\Delta\bar{W} - N_f$  curve actually is closer to  $k \approx 1.7$ .

In any regard, welds and welded joints are highly irregular in nature. It is therefore nearly, if not impossible to produce two specimens with the same exact geometry. Because of this phenomenon, teasing two specimens with the same joint geometry at the same stress level might result in two different fatigue lives. An aspect, which then leads to scattering in the experimental results. It is therefore essential that when the goal is to produce an accurate fatigue criterion, that a sufficient amount of specimens are considered. With a large number of specimens considered, the mean value for both geometric parameters and then the resultant  $\Delta\bar{W}$  will yield a more accurate prediction of the fatigue life expectancy.

### **Evaluation of the analytical results**

The analytical evaluation of ASED is more of a control of the model, the parameters and the method used in the FEA than a control of ASED as a fatigue criterion for AZ31 magnesium alloy. Because both the SIF and the max stress ( $\sigma_{max}$ ) are parameters which are extracted from the same FEM model as the  $\Delta\bar{W}$ . Nevertheless, it is a valuable assessment, which gives an excellent insight to the accuracy of ASED.

The analytical assessment of ASED as a fatigue criterion for AZ31, with the aid of equations based on SIF, has proven to be a viable approach, as is apparent from figure 5.12. The resultant  $\Delta\bar{W} - N_f$  plot yielded a good regressions fit ( $R^2 = 0.56$ ) regardless of loading ratio. In figure 6.2 the analytically obtained data for  $\Delta\bar{W} - N_f$  is overlaid that which was obtained through the numerical investigation (both for the non-penetrated butt welded joint). It shows that the discrepancy between the two are modest, and is at  $\sim 11.8\%$ . The slope and fit to the power law regression line are identical for the two. It is important to acknowledge that the SIF used was obtained through the use of  $\sim 1500$  elements, and the  $\Delta\bar{W}$ , on the other hand, was obtained with 40 elements, a ratio of 1 : 37.5.

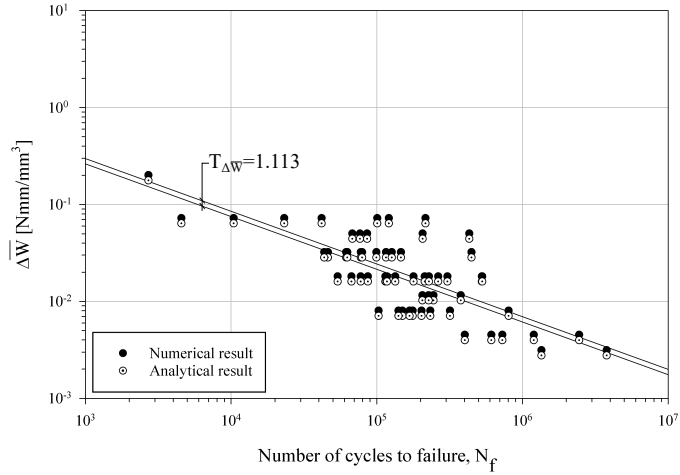


**Figure 6.2:** Comparison of analytically derived  $\Delta\bar{W} - N_f$  and numerically derived  $\Delta\bar{W} - N_f$

The comparison between maximum notch stress found numerically and analytically also indicates that the agreement between the two is good. As shown in table 5.1 the discrepancy between the two is only at 8.06%. When comparing the number of elements used in the two approaches, we get a ratio of 1 : 100. This means that for every one element used in the ASFD FEA, there is used 100 elements in the FEA where the  $\sigma_{max}$  was obtained.

### Evaluation of the control radius

Ideally, the control radius  $R_c$  for ASFD as a fatigue criterion is obtained analytically by equation 2.20. As the necessary fatigue parameters for an un-notched specimen was unavailable, the approach of "best-fit" was utilized to determine an appropriate  $R_c$  for welded joints of AZ31 magnesium alloy. The reference point for this method was the  $R_c$  used for welded aluminum alloy found in the literature. The selected  $R_c$  which yielded the best regression fit was found to be  $R_c = 0.15 \text{ mm}$ .

A further study of the effect of  $R_c$  on the extracted  $\Delta\bar{W}$  is shown in figure 6.3. In this study, the three geometries were loaded to their respective fatigue strength at  $N_f = 2 \cdot 10^6$  ( $R=0$ ), and then multiple analysis with incrementally changing  $R_c$  was conducted. If a perfect  $R_c$  for AZ31 magnesium alloy were to be established by this method, the resultant  $\Delta\bar{W}$  for all geometries would intercept at one point, in which the appropriate  $R_c$  would be. As the study in 6.3 shows, the resultant  $\Delta\bar{W}$  for the three geometries are near parallel, and will most likely never intercept each other. In other words, using the three geometries considered in this investigation, it will not be feasible to establish a correct  $R_c$  for AZ31 magnesium alloy.

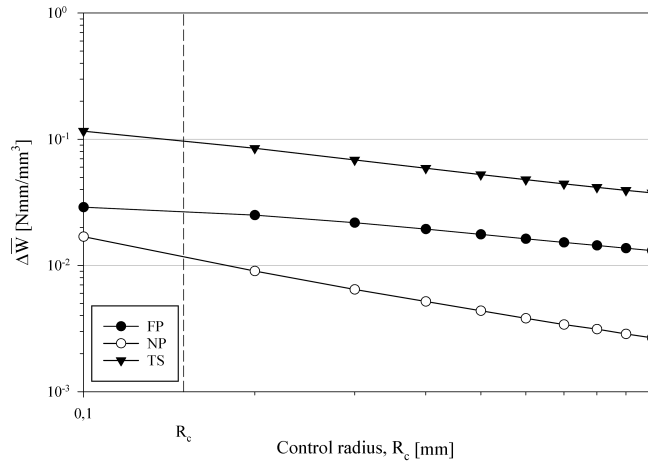


**Figure 6.3:** Plot of the effect of altering the control radius on the resultant  $\Delta\bar{W}$  when specimens are applied with their respective fatigue strength at  $N_f = 2 \cdot 10^6$  at  $R=0$ . FP = Fully penetrated butt welded plate; NP = Non-penetrated butt welded plate; TS: Plate with welded transverse stiffener.  $R_c = 0.15 \text{ mm}$

The  $R_c$  that was established as the best fit for AZ31 magnesium alloy given the available data is also indicated in figure 6.3. As can be seen, the applied  $R_c$  is at a "middle ground" point where the discrepancy between the three resultant  $\Delta\bar{W}$  versus  $R_c$  are the smallest. Also apparent is that for the fully penetrated butt weld and the non-penetrated butt weld, as the  $R_c$  is reduced from 0.20 mm to 0.10 mm, the discrepancy between the two start to decrease. This indicates that an even smaller  $R_c$  than 0.15 mm might be applicable for AZ31 magnesium alloy if other geometries are investigated.

# Chapter 7

## Conclusion

The scope of this thesis was to apply the energy-based fatigue criterion ASED to welded joints made of AZ31 magnesium alloy. This evaluation was done through a numerical investigation which was based on experimental data. Three joint geometries were investigated, namely: plate with fully penetrated butt weld, plate with non-penetrated butt weld and plate with transverse stiffener. These joints were tested under three different loading rates of  $R=-1$ ,  $R=0$ , and  $R=0.5$ .

Through the experimental investigation it was found that when subjecting the welded joints to a cyclical load, the geometry of the joint and the mean applied stress, significantly affected its expected fatigue life. This is believed to be due to the geometry of the weld toe, and weld root, as these generate different amounts of stress concentrations depending on their size and geometry. Hence, a higher stress concentration generally causes the failure to occur earlier, compared to a lower one.

In the process of applying ASED as a new fatigue criterion for AZ31, attention to the parameters to be used in the numerical investigation was taken. It was found that due to the blunt weld toe of the fully penetrated butt weld and the fillet weld on the transverse stiffener, the control radius  $R_c$  had to be compensated with the parameter  $r_0 = 0.33 \text{ mm}$  and  $r_0 = 0.12 \text{ mm}$ , respectively. The control radius used in the numerical investigation was obtained through an iteration approach.  $\Delta\bar{W}$  was extracted for all geometries under a pulsating load ( $R=0$ ), with an incrementally changing  $R_c$ . The  $R_c$  that yielded the best regressions fit between the geometries was selected to be the appropriate one, resulting in a control radius of  $R_c = 0.15 \text{ mm}$ . In addition, a mesh-sensitivity study was conducted to ensure that an adequate amount of elements within the control radius was selected. After the appropriate parameters for each geometry was established, multiple analysis were performed with the stress range found experimentally. The resultant  $\Delta\bar{W}$  was then compared with its respective number of cycles to failure. The results of the analysis were then plotted with double logarithmic scale and fitted with a power law regression.

To verify the results from the numerical model, an analytical evaluation based on equations found in the literature was performed. The evaluation was performed for the non-penetrated butt weld and was based on stress intensity. In addition, an evaluation of the occurring max stress at the weld toe for the fully penetrated butt weld was performed. This evaluation gave valuable insight into the accuracy of ASED. The discrepancy between the numerical and analytical results was found to be 11.8% for the evaluation base on SIF and 8.06% for the one based on the occurring weld toe max stress. It is important to acknowledge that the ratio of elements used in the FEA to extract SIF and the max stress was 1 : 37.5 and 1 : 100. In other words, for every one element used in the ASED-based FEA, a hundred elements have to be used in the stress-based FEA. Which is indeed a statement to the benefits of using ASED.

The resultant plots of  $\Delta\bar{W} - N_f$  indicate that when applying ASED as a fatigue criterion the relationship between  $\Delta\bar{W}$  and  $N_f$  follows a power law trend. The results also show that there is a relatively large scatter in the results ( $T_{\Delta\bar{W}} \approx 30$  for the global plot), when compared to the results of investigations on other materials with similar properties. Because of this scatter in the result amongst the geometries it is difficult to determine, with certainty, a correct slope for the global power law regression line.

In conclusion, based on the results from the work conducted in this thesis, it is believed that the use of ASED as a fatigue criterion for welded joints made of AZ31 magnesium alloy is a viable approach. Although, further research has to be performed so that parametric constants are established and more experimental data considered, and thereby increasing the accuracy of fatigue life prediction.

## 7.1 Further work

As the work conducted in this thesis was the first study into the application of ASED as a fatigue criterion for welded joint of AZ31 magnesium alloy, there still is additional research needed before this method can be applied in engineering. Some important research points are:

- Obtain a control radius through the use of an analytical approach: the suggested best practice to obtain a control radius according to the literature is through assessing the experimental fatigue data of a welded specimen where the welds are ground flush (i.e., a smooth specimen). Therefore it is recommended that if further research on applying ASED as a fatigue criterion is conducted, an assessment on the fatigue properties of smooth specimens is performed, and thus obtaining the necessary experimental data to calculate  $R_c$  analytically.
- Further experimental testing: if to improve the accuracy of predicting fatigue life using ASED as a fatigue criterion, more experimental data have to be considered. This meaning that specimens with other geometries than that of the ones that have already been evaluated should also be considered. Geometries such as a single lap joint and/or a crucifix shape (which is often considered in the literature). It is essential that if further experimental investigation is to be conducted, that accurate measurements of critical features is done. These accurate measurements will aid in developing a numerical model which can better recreate the actual occurring stresses that a specimen experiences under loading.
- Study the effect of mixed mode loading: it would be a valuable insight to see the impact of mixed mode loading on ASED, and how it influences its accuracy as a fatigue criterion for AZ31.

# Bibliography

- [1] R. Lee, “The Outlook for Population Growth,” *Science*, vol. 333, no. November, pp. 569–573, 2011.
- [2] P.A. Withey, “Fatigue failure of the de Havilland comet I,” *Engineering Failure Analysis*, vol. 4, pp. 147–154, 6 1997.
- [3] P. Lazzarin, F. Berto, F. J. Gomez, and M. Zappalorto, “Some advantages derived from the use of the strain energy density over a control volume in fatigue strength assessments of welded joints,” *International Journal of Fatigue*, vol. 30, no. 8, pp. 1345–1357, 2008.
- [4] P. Livieri and P. Lazzarin, “Fatigue strength of steel and aluminium welded joints based on generalised stress intensity factors and local strain energy values,” *International Journal of Fracture*, vol. 133, no. 3, pp. 247–276, 2005.
- [5] P. Lazzarin, P. Livieri, F. Berto, and M. Zappalorto, “Local strain energy density and fatigue strength of welded joints under uniaxial and multiaxial loading,” *Engineering Fracture Mechanics*, vol. 75, no. 7, pp. 1875–1889, 2008.
- [6] I. A. Ashcroft and A. D. Crocombe, “Modelling Fatigue in Adhesively Bonded Joints,” in *Modeling of Adhesively Bonded Joints* (L. F. M. da Silva and A. Öchsner, eds.), ch. 7, pp. 183–223, Springer-Verlag Berlin Heidelberg, 1 ed., 2008.
- [7] N. E. Dowling, “Fatigue of Materials: Introduction and Stress-Based Approach,” in *Mechanical Behavior of Materials*, ch. 9, pp. 468–470, Pearson Education Limited, 4 ed., 2013.
- [8] E. Oberg, F. D. Jones, H. L. Horton, and H. H. Ryffel, “Welding,” in *Machinery’s handbook*, ch. 57, pp. 1496–1549, Industrial Press, Inc., 30 ed., 2016.
- [9] D. Kaplan and G. Murry, “Thermal, Metallurgical and Mechanical Phenomena in the Heat Affected Zone,” in *Metallurgy and Mechanics of Welding* (R. Blondeau, ed.), pp. 89–131, London, UK: ISTE, 2010.
- [10] E. Halmøy, “Introduksjon,” in *Sveiseteknikk*, pp. 1–14, Institutt For Produktutvikling og Produksjon, Norwegian University of Science and Technology, 2007.
- [11] E. Halmøy, “Noen sveisetekniske begreper,” in *Sveiseteknikk*, ch. 1, pp. 6–10, Institutt For Produktutvikling og Produksjon, Norwegian University of Science and Technology, 2017.
- [12] T. Anderson, “Linear elastic fracture mechanics,” in *Fracture Mechanics*, ch. 2, pp. 70–73, CRC Press, 2nd ed. ed., 1995.
- [13] M. R. Ayatollahi, M. Rashidi Moghaddam, S. M. Razavi, and F. Berto, “Geometry effects on fracture trajectory of PMMA samples under pure mode-I loading,” *Engineering Fracture Mechanics*, vol. 163, pp. 449–461, 2016.

- 
- [14] C. Sun and Z.-H. Jin, "Introduction," in *Fracture Mechanics*, pp. 1–10, Elsevier, 2012.
- [15] G. R. Irwin, "Analysis of Stresses and Strains Near the End of a Crack Traversing a Plate," *Journal of applied mechanics*, no. 24, pp. 361–364, 1957.
- [16] L. G. Zhao, J. Tong, and J. Byrne, "Stress intensity factor K and the elastic T-stress for corner cracks," *International Journal of Fracture*, vol. 109, no. 2, pp. 209–225, 2001.
- [17] C. Sun and Z.-H. Jin, "The Elastic Stress Field around a Crack Tip," in *Fracture Mechanics*, ch. 3, pp. 25–75, Elsevier, 2012.
- [18] A. A. Griffith, "The Phenomena of Rupture and Flow in Solids," *Philos Trans R Soc Lond A221*, vol. 221, pp. 163–198, 1920.
- [19] P. Lazzarin and S. Filippi, "A generalized stress intensity factor to be applied to rounded V-shaped notches," *International Journal of Solids and Structures*, vol. 43, no. 9, pp. 2461–2478, 2006.
- [20] P. Lazzarin and R. Tovo, "A unified approach to the evaluation of linear elastic stress fields in the neighborhood of cracks and notches," *International Journal of Fracture*, vol. 78, no. 1, pp. 3–19, 1996.
- [21] M. P. Savruk and A. Kazberuk, "Problems of fracture mechanics of solid bodies with V-shaped notches," *Materials Science*, vol. 45, no. 2, pp. 162–180, 2009.
- [22] M. P. Savruk and A. Kazberuk, "Stress Distribution in Elastic Plane with a Semi-infinite Notch," in *Stress Concentration at Notches*, ch. 2, pp. 57–60, Cham: Springer International Publishing, 2017.
- [23] G. Sih, "Some basic problems in fracture mechanics and new concepts," *Engineering Fracture Mechanics*, vol. 5, no. 2, pp. 365–377, 1973.
- [24] A. T. Zehnder, "Strain Energy Density Failure Criterion: Mixed-Mode Crack Growth," in *Fracture Mechanics*, vol. 62 of *Lecture Notes in Applied and Computational Mechanics*, ch. 7, pp. 195–238, Dordrecht: Springer Netherlands, 2012.
- [25] H. Göldner, "Neuber, H., Kerbspannungslehre. 3., erw. Auflage. Theorie der Spannungskonzentration. Genaue Berechnung der Festigkeit. Berlin-Heidelberg-New York-Tokyo, Springer-Verlag 1985. XI, 326 S., 214 Abb., DM 198,—. ISBN 3-540-13558-8," *ZAMM - Journal of Applied Mathematics and Mechanics / Zeitschrift für Angewandte Mathematik und Mechanik*, vol. 66, no. 7, pp. 319–319, 1986.
- [26] F. Berto, A. Campagnolo, and P. Lazzarin, "Fatigue strength of severely notched specimens made of Ti-6Al-4V under multiaxial loading," *Fatigue and Fracture of Engineering Materials and Structures*, vol. 38, no. 5, pp. 503–517, 2015.

- 
- [27] P. Lazzarin, F. Berto, M. Elices, and J. Gómez, “Brittle failures from U- and V-notches in mode I and mixed, I + II, mode: A synthesis based on the strain energy density averaged on finite-size volumes,” *Fatigue and Fracture of Engineering Materials and Structures*, vol. 32, no. 8, pp. 671–684, 2009.
- [28] F. J. Gómez, M. Elices, F. Berto, and P. Lazzarin, “Local strain energy to assess the static failure of U-notches in plates under mixed mode loading,” *International Journal of Fracture*, vol. 145, no. 1, pp. 29–45, 2007.
- [29] P. Lazzarin and R. Zambardi, “A finite-volume-energy based approach to predict the static and fatigue behavior of components with sharp V-shaped notches,” *International Journal of Fracture*, vol. 112, no. 3, pp. 275–298, 2001.
- [30] P. Lazzarin, F. Berto, and M. Zappalorto, “Rapid calculations of notch stress intensity factors based on averaged strain energy density from coarse meshes: Theoretical bases and applications,” *International Journal of Fatigue*, vol. 32, no. 10, pp. 1559–1567, 2010.
- [31] R. N. Katz, M. M. Makhlof, and I. Introduction, “Aluminum Alloys,” vol. 31, no. February, pp. 30–34, 2000.
- [32] T. K. Aune, H. Gjestland, J. Haagenen, B. Kittilsen, J. I. Skar, and H. Westengen, “Magnesium Alloys,” in *Ullmann’s Encyclopedia of Industrial Chemistry*, Weinheim, Germany: Wiley-VCH Verlag GmbH & Co. KGaA, 1 2003.
- [33] Karakas, C. Morgenstern, and C. M. Sonsino, “Fatigue design of welded joints from the wrought magnesium alloy AZ31 by the local stress concept with the fictitious notch radii of  $r_f = 1.0$  and  $0.05$  mm,” *International Journal of Fatigue*, vol. 30, no. 12, pp. 2210–2219, 2008.
- [34] Karakas, “Consideration of mean-stress effects on fatigue life of welded magnesium joints by the application of the Smith-Watson-Topper and reference radius concepts,” *International Journal of Fatigue*, vol. 49, pp. 1–17, 2013.
- [35] Karakaş, G. Zhang, and C. M. Sonsino, “Critical distance approach for the fatigue strength assessment of magnesium welded joints in contrast to Neuber’s effective stress method,” *International Journal of Fatigue*, vol. 112, no. March, pp. 21–35, 2018.
- [36] M. Tsujikawa, H. Somekawa, K. Higashi, H. Iwasaki, T. Hasegawa, and A. Mizuta, “Fatigue of Welded Magnesium Alloy Joints,” *Materials Transactions*, vol. 45, no. 2, pp. 419–422, 2004.
- [37] Karakaş, “Application of Neuber’s effective stress method for the evaluation of the fatigue behaviour of magnesium welds,” *International Journal of Fatigue*, vol. 101, pp. 115–126, 2017.
- [38] O. Karakas, A. Gülsöz, H. Kaufmann, and C. M. Sonsino, “Fatigue behaviour of welded joints from magnesium alloy (AZ31) according to the local strain concept,” *Materialwissenschaft und Werkstofftechnik*, vol. 41, no. 2, pp. 73–82, 2010.
-

- 
- [39] O. Karakas, A. Gülsöz, H. Kaufmann, and C. M. Sonsino, "Fatigue behaviour of welded joints from magnesium alloy (AZ31) according to the local strain concept," *Materialwissenschaft und Werkstofftechnik*, vol. 41, no. 2, pp. 73–82, 2010.
- [40] A. M. Easley, Joe G. ; Waas, "Displacement, Strain, and Material Properties," in *Analysis of Structures*, ch. 3, p. 90, Chichester, UK: John Wiley & Sons, Ltd, 8 2011.
- [41] ABAQUS, "Abaqus user manual - 17.6.1 Verifying your mesh," 2006.
- [42] P. Lazzarin and F. Berto, "Some expressions for the strain energy in a finite volume surrounding the root of blunt V-notches," *International Journal of Fracture*, vol. 135, no. 1-4, pp. 161–185, 2005.
- [43] Azom.com, "Magnesium AZ31 Alloy, data sheet," 2012.
- [44] T. Sasaki, H. Somekawa, A. Takara, Y. Nishikawa, and K. Higashi, "Plane-Strain Fracture Toughness on Thin AZ31 Wrought Magnesium Alloy Sheets," *Materials Transactions*, vol. 44, no. 5, pp. 986–990, 2003.

# Appendix



# Appendix A

## Notch opening angle variables

**Table A.1:** Notch opening angle variables. Some excerpt of tables from the paper *Some expressions for the strain energy in a finite volume surrounding the root of blunt V-notches* by P. Lazzarin and F. Berto (2005) [42]

Excerpt from <i>Table 1</i>		
$2\alpha$		$F(2\alpha)$
$0^\circ$		0.7850
$120^\circ$		1.3334
$135^\circ$		1.2500
Excerpt from <i>Table 2</i>		
$\gamma/\pi$ (rad)	$I_1(\gamma)$	$\nu = 0.35$
0		0.7425
$\frac{2}{3}$		0.6184
$\frac{5}{8}$		0.5796
Excerpt from <i>Table 3</i>		
$2\alpha$	$\frac{H}{R_0/\rho}$	$\nu = 0.35$
$0^\circ$	1	0.5432
$120^\circ$	0.1	0.3767
	1	0.1079
$135^\circ$	0.1	0.3082
	1	0.0988

---

---

## Appendix B

# AZ31 Magnesium Alloy material properties

**Table B.1:** Monotonic and cyclic material properties of AZ31 magnesium alloy [34], <sup>1</sup>[43], <sup>2</sup> [44]

Parameter	Base material	Weld material	Heat affected zone
Density	1.77 g/cm <sup>3</sup>	-	-
Young's modulus, $E$	43 GPa	37 GPa	43 GPa
Tensile strength <sup>1</sup> , $\sigma_U$	260 MPa	-	-
Fracture toughness <sup>2</sup> , $K_{Ic}$	18.4 MPa $\sqrt{m}$	-	-
Monotonic strength coefficient, $K$	900 MPa	583 MPa	723 MPa
Monotonic strain hardening exponent, $n$	0.211	0.271	0.182
Monotonic yield strength, $R_{p0.2}$	240 MPa	108 MPa	233 MPa
Cyclic yield strength, $R'_{p0.2}$	200 MPa	129 MPa	227 MPa
Cyclic strength coefficient, $K'$	317 MPa	428 MPa	615 MPa
Cyclic strain hardening exponent, $n'$	0.073	0.193	0.161
Fatigue strength coefficient, $\sigma'_f$	104.3 MPa	53.0 MPa	1150.4 MPa
Fatigue strength exponent, $b$	-0.201	-0.172	-0.204
Fatigue ductility coefficient, $\epsilon'_f$	19.2	16.3	2006.1
Fatigue ductility exponent, $c$	-0.789	-0.721	-1.365

---

---

## Appendix C

# Experimental and numerical results

**Table C.1:** Fully penetrated butt welded plate, R = -1

Sample nr.	$\sigma_a$ [MPa]	$\Delta\sigma$ [MPa]	$N_f$	$\Delta\bar{W}$ [Nmm/mm <sup>3</sup> ]
DV 2	25,0	25,0	Run-out	1,30E-02
DV 19	20,0	20,0	Run-out	8,30E-03
DV 64	20,0	20,0	Run-out	8,30E-03
DV 28	20,0	20,0	Run-out	8,30E-03
DV 38	22,5	22,5	Run-out	1,05E-02
DV 56	25,0	25,0	292 651	1,30E-02
DV 69	25,0	25,0	407 567	1,30E-02
DV 47	25,0	25,0	909 206	1,30E-02
DV 50	20,0	20,0	683 752	8,30E-03
DV 41	27,5	27,5	407 944	1,57E-02
DV 34	40,0	40,0	149 093	3,32E-02
DV 3	40,0	40,0	177 354	3,32E-02
DV 40	40,0	40,0	250 355	3,32E-02
DV 29	40,0	40,0	238 381	3,32E-02
DV 18	50,0	50,0	65 535	5,19E-02
DV 49	50,0	50,0	61 328	5,19E-02
DV 2	50,0	50,0	106 435	5,19E-02
DV 19	50,0	50,0	115 826	5,19E-02
DV 33	60,0	60,0	67 122	7,47E-02
DV 51	60,0	60,0	26 433	7,47E-02
DVoWS 1	50,0	50,0	107 465	5,19E-02
DVoWS 2	50,0	50,0	116 686	5,19E-02
DVoWS 3	25,0	25,0	440 010	1,30E-02
DVoWS 4	25,0	25,0	407 432	1,30E-02

**Table C.2:** Fully penetrated butt welded plate, R = 0

Sample nr.	$\sigma_a$ [MPa]	$\Delta\sigma$ [MPa]	$N_f$	$\Delta\bar{W}$ [Nmm/mm <sup>3</sup> ]
DV 139	10,0	20	Run-out	8,30E-03
DV 146	15,0	30	Run-out	1,87E-02
DV 136	20,0	40	Run-out	3,32E-02
DV 123	15,0	30	1 008 991	1,87E-02
DV 137	20,0	40	478 114	3,32E-02
DV 138	20,0	40	378 586	3,32E-02
DV 148	20,0	40	610 932	3,32E-02
DV 78	20,0	40	552 848	3,32E-02
DV 48	20,0	40	353 648	3,32E-02
DV 61	20,0	40	308 655	3,32E-02
DV 136	30,0	60	296 979	7,47E-02
DV 139	30,0	60	181 788	7,47E-02
DV 93	30,0	60	116 272	7,47E-02
DV 89	30,0	60	70 778	7,47E-02
DV 79	30,0	60	100 492	7,47E-02
DV 146	40,0	80	76 373	1,33E-01
DV 155	40,0	80	37 390	1,33E-01
DV 135	40,0	80	54 598	1,33E-01
DV 149	40,0	80	50 291	1,33E-01
DVoWS 5	20,0	40	320 450	3,32E-02
DVoWS 6	40,0	80	63 970	1,33E-01
DVoWS 7	40,0	80	55 609	1,33E-01
DVoWS 8	20,0	40	430 687	3,32E-02

**Table C.3:** Fully penetrated butt welded plate, R = 0.5

Sample nr.	$\sigma_a$ [MPa]	$\Delta\sigma$ [MPa]	$N_f$	$\Delta\bar{W}$ [Nmm/mm <sup>3</sup> ]
90	15,0	30,0	1 366 910	1,87E-02
68	17,0	34,0	549 536	2,40E-02
65	17,0	34,0	307 545	2,40E-02
94	20,0	40,0	268 418	3,32E-02
134	30,0	60,0	67 752	7,47E-02
SVoWS0.5-77	30,0	60,0	35 986	7,47E-02
SVoWS0.5-99	30,0	60,0	74 830	7,47E-02
SVoWS0.5-126	20,0	40,0	286 971	3,32E-02
SVoWS0.5-129	20,0	40,0	274 627	3,32E-02

**Table C.4:** Non-penetrated butt welded plate, R = -1

Sample nr.	$\sigma_a$ [MPa]	$\Delta\sigma$ [MPa]	$N_f$	$\Delta\bar{W}$ [Nmm/mm <sup>3</sup> ]
13	5,0	5,0	Run-out	2,02E-03
15	5,0	5,0	Run-out	2,02E-03
9	7,5	7,5	Run-out	4,55E-03
6	50,0	50,0	2702	2,02E-01
3	30,0	30,0	10384	7,28E-02
1	15,0	15,0	53699	1,82E-02
37	15,0	15,0	114555	1,82E-02
27	15,0	15,0	86812	1,82E-02
10	15,0	15,0	115239	1,82E-02
17	15,0	15,0	77567	1,82E-02
31	15,0	15,0	117345	1,82E-02
16	10,0	10,0	232706	8,09E-03
34	10,0	10,0	176243	8,09E-03
14	10,0	10,0	102918	8,09E-03
21	10,0	10,0	149866	8,09E-03
24	10,0	10,0	167895	8,09E-03
29	10,0	10,0	140709	8,09E-03
30	7,5	7,5	611662	4,55E-03
7	7,5	7,5	1194395	4,55E-03
18	7,5	7,5	401549	4,55E-03
36	7,5	7,5	726337	4,55E-03
12	7,5	7,5	2451389	4,55E-03
22	6,3	6,3	3780048	3,16E-03
40	6,3	6,3	1347736	3,16E-03
DVmWS 1	15,0	15,0	66815	1,82E-02
DVmWS 2	10,0	10,0	317779	8,09E-03
DVmWS 3	15,0	15,0	133864	1,82E-02
DVmWS 4	10,0	10,0	202582	8,09E-03

**Table C.5:** Non-penetrated butt welded plate, R = 0

Sample nr.	$\sigma_a$ [MPa]	$\Delta\sigma$ [MPa]	$N_f$	$\Delta\bar{W}$ [Nmm/mm <sup>3</sup> ]
57	5,0	10,0	Run-out	8,09E-03
58	5,0	10,0	Run-out	8,09E-03
62	5,0	10,0	Run-out	8,09E-03
69	7,5	15,0	Run-out	1,82E-02
57	15,0	30,0	4 542	7,28E-02
69	15,0	30,0	100 700	7,28E-02
71	15,0	30,0	23 104	7,28E-02
63	15,0	30,0	120 870	7,28E-02
78	15,0	30,0	41 712	7,28E-02
73	15,0	30,0	215 862	7,28E-02
62	12,5	25,0	67 924	5,05E-02
76	12,5	25,0	76 684	5,05E-02
61	12,5	25,0	85 754	5,05E-02
67	12,5	25,0	206 420	5,05E-02
58	12,5	25,0	431 136	5,05E-02
52	10,0	20,0	46 063	3,23E-02
45	10,0	20,0	61 525	3,23E-02
50	10,0	20,0	99 253	3,23E-02
77	10,0	20,0	115 602	3,23E-02
70	10,0	20,0	446 826	3,23E-02
53	7,5	15,0	178 506	1,82E-02
74	7,5	15,0	213 393	1,82E-02
72	7,5	15,0	305 451	1,82E-02
44	7,5	15,0	526 353	1,82E-02
75	7,5	15,0	228 048	1,82E-02
51	5,0	10,0	803 334	8,09E-03
DVmWS 5	10,0	20,0	126 642	3,23E-02
DVmWS 6	10,0	20,0	77 634	3,23E-02
DVmWS 7	7,5	15,0	263 855	1,82E-02
DVmWS 8	7,5	15,0	528 629	1,82E-02

---

**Table C.6:** Non-penetrated butt welded plate, R = 0.5

Sample nr.	$\sigma_a$ [MPa]	$\Delta\sigma_{max}$ [MPa]	$N_f$	$\Delta\bar{W}$ [Nmm/mm <sup>3</sup> ]
A 13	6,0	12,0	205 567	1,16E-02
A18	6,0	12,0	244 742	1,16E-02
A 15	10,0	20,0	146 461	3,23E-02
A 12	10,0	20,0	62 549	3,23E-02
DVmWS 9	10,0	20,0	79 168	3,23E-02
DVmWS 10	10,0	20,0	43 436	3,23E-02
DVmWS 11	6,0	12,0	376 530	1,16E-02
DVmWS 12	6,0	12,0	227 086	1,16E-02

---

**Table C.7:** Plate with welded transverse stiffener, R = -1

Sample nr.	$\sigma_a$ [MPa]	$\Delta\sigma$ [MPa]	$N_f$	$\Delta\bar{W}$ [Nmm/mm <sup>3</sup> ]
42	25,0	25,0	Run-out	2,10E-02
44	30,0	30,0	Run-out	3,02E-02
22	30,0	30,0	Run-out	3,02E-02
93	30,0	30,0	Run-out	3,02E-02
62	30,0	30,0	Run-out	3,02E-02
24	35,0	35,0	975 846	4,12E-02
12	35,0	35,0	1 029 596	4,12E-02
29	35,0	35,0	1 114 680	4,12E-02
91	35,0	35,0	1 216 794	4,12E-02
87	40,0	40,0	466 924	5,37E-02
94	40,0	40,0	566 193	5,37E-02
72	40,0	40,0	607 834	5,37E-02
83	40,0	40,0	742 040	5,37E-02
45	40,0	40,0	754 843	5,37E-02
43	40,0	40,0	896 367	5,37E-02
62	50,0	50,0	273 027	8,40E-02
81	50,0	50,0	289 282	8,40E-02
37	50,0	50,0	291 621	8,40E-02
77	50,0	50,0	308 821	8,40E-02
17	50,0	50,0	343 353	8,40E-02
76	50,0	50,0	289 038	8,40E-02
46	60,0	60,0	141 731	1,21E-01
41	60,0	60,0	147 660	1,21E-01
93	60,0	60,0	170 436	1,21E-01
52	60,0	60,0	182 590	1,21E-01
74	60,0	60,0	199 369	1,21E-01
65	60,0	60,0	231 011	1,21E-01
QS 1.40	40,0	40,0	378 372	5,37E-02
QS 1.68	60,0	60,0	210 126	1,21E-01

**Table C.8:** Plate with welded transverse stiffener, R = 0

Sample nr.	$\sigma_a$ [MPa]	$\Delta\sigma$ [MPa]	$N_f$	$\Delta\bar{W}$ [Nmm/mm <sup>3</sup> ]
24	25,0	50,0	Run-out	8,4E-02
23	15,0	30,0	Run-out	3,0E-02
50	20,0	40,0	Run-out	5,4E-02
59	25,0	50,0	Run-out	8,4E-02
44	25,0	50,0	Run-out	8,4E-02
13	25,0	50,0	645 904	8,4E-02
28	25,0	50,0	1 255 713	8,4E-02
30	25,0	50,0	1 558 574	8,4E-02
27	30,0	60,0	207 707	1,2E-01
98	30,0	60,0	271 990	1,2E-01
59	30,0	60,0	295 339	1,2E-01
49	30,0	60,0	312 472	1,2E-01
44	30,0	60,0	359 078	1,2E-01
15	30,0	60,0	364 448	1,2E-01
80	40,0	80,0	125 092	2,1E-01
99	40,0	80,0	135 295	2,1E-01
91	40,0	80,0	144 131	2,1E-01
43	40,0	80,0	147 356	2,1E-01
58	40,0	80,0	162 932	2,1E-01
34	40,0	80,0	179 568	2,1E-01
25	50,0	100,0	53 223	3,4E-01
61	50,0	100,0	74 532	3,4E-01
63	50,0	100,0	74 698	3,4E-01
39	50,0	100,0	75 750	3,4E-01
71	50,0	100,0	77 821	3,4E-01
90	50,0	100,0	78 628	3,4E-01
QS 0.18	50,0	100,0	60 790	3,4E-01
QS 0.79	30,0	60,0	284 488	1,2E-01

---

**Table C.9:** Plate with welded transverse stiffener, R = 0.5

Sample nr.	$\sigma_a$ [MPa]	$\sigma_{max}$ [MPa]	$N_f$	$\Delta\bar{W}$ [Nmm/mm <sup>3</sup> ]
85	18,0	36,0	533 109	4,354E-02
53	20,0	40,0	618 922	5,375E-02
16	20,0	40,0	283 500	5,375E-02
69	30,0	60,0	88 134	1,209E-01
64	40,0	80,0	28 364	2,150E-01
QS 0,5-84	40,0	80,0	38 071	2,150E-01
QS 0,5-66	20,0	40,0	266 730	5,375E-02
QS 0,5-75	20,0	40,0	291 014	5,375E-02
QS 0,5-95	40,0	80,0	51 199	2,150E-01
QS 0,5-72	30,0	60,0	91 266	1,209E-01
QS 0,5-89	30,0	60,0	108 154	1,209E-01
QS 0,5-73	18,0	36,0	596 345	4,354E-02
QS 0,5-78	18,0	36,0	430 569	4,354E-02
QS 0,5-96	15,0	30,0	5 000 000	3,023E-02

---

# Appendix D

## Results from analytical investigation

**Table D.1:** Analytical results for non-penetrated butt welded plate, R=-1

$\sigma_a$ [MPa]	$\Delta\sigma$ [MPa]	$N_f$	$\Delta\bar{W}$ [ $Nmm/mm^3$ ]
50,0	50,0	2 702	1,78E-01
30,0	30,0	10 384	6,42E-02
15,0	15,0	53 699	1,61E-02
15,0	15,0	114 555	1,61E-02
15,0	15,0	86 812	1,61E-02
15,0	15,0	115 239	1,61E-02
15,0	15,0	77 567	1,61E-02
15,0	15,0	117 345	1,61E-02
10,0	10,0	232 706	7,13E-03
10,0	10,0	176 243	7,13E-03
10,0	10,0	102 918	7,13E-03
10,0	10,0	149 866	7,13E-03
10,0	10,0	167 895	7,13E-03
10,0	10,0	140 709	7,13E-03
7,5	7,5	611 662	4,01E-03
7,5	7,5	1 194 395	4,01E-03
7,5	7,5	401 549	4,01E-03
7,5	7,5	726 337	4,01E-03
7,5	7,5	2 451 389	4,01E-03
6,3	6,3	3 780 048	2,79E-03
6,3	6,3	1 347 736	2,79E-03
15,0	15,0	66 815	1,61E-02
10,0	10,0	317 779	7,13E-03
15,0	15,0	133 864	1,61E-02
10,0	10,0	202 582	7,13E-03

**Table D.2:** Analytical results for non-penetrated butt welded plate, R=0

$\sigma_a$ [MPa]	$\Delta\sigma$ [MPa]	$N_f$	$\Delta\bar{W}$ [ $Nmm/mm^3$ ]
15,0	30,0	4 542	6,42E-02
15,0	30,0	100 700	6,42E-02
15,0	30,0	23 104	6,42E-02
15,0	30,0	120 870	6,42E-02
15,0	30,0	41 712	6,42E-02
15,0	30,0	215 862	6,42E-02
12,5	25,0	67 924	4,46E-02
12,5	25,0	76 684	4,46E-02
12,5	25,0	85 754	4,46E-02
12,5	25,0	206 420	4,46E-02
12,5	25,0	431 136	4,46E-02
10,0	20,0	46 063	2,85E-02
10,0	20,0	61 525	2,85E-02
10,0	20,0	99 253	2,85E-02
10,0	20,0	115 602	2,85E-02
10,0	20,0	446 826	2,85E-02
7,5	15,0	178 506	1,61E-02
7,5	15,0	213 393	1,61E-02
7,5	15,0	305 451	1,61E-02
7,5	15,0	526 353	1,61E-02
7,5	15,0	228 048	1,61E-02
5,0	10,0	803 334	7,13E-03
10,0	20,0	126 642	2,85E-02
10,0	20,0	77 634	2,85E-02
7,5	15,0	263 855	1,61E-02
7,5	15,0	528 629	1,61E-02

**Table D.3:** Analytical results for non-penetrated butt welded plate, R=0.5

$\sigma_a$ [MPa]	$\Delta\sigma$ [MPa]	$N_f$	$\Delta\bar{W}$ [ $Nmm/mm^3$ ]
6,0	12,0	205 567	1,03E-02
6,0	12,0	244 742	1,03E-02
10,0	20,0	146 461	2,85E-02
10,0	20,0	62 549	2,85E-02
10,0	20,0	79 168	2,85E-02
10,0	20,0	43 436	2,85E-02
6,0	12,0	376 530	1,03E-02
6,0	12,0	227 086	1,03E-02